CORE
Metadata, citation and similar papers at core.ac.uk
Provided by Brunel University Research Archive

Phase Field Approach to Heterogeneous Crystal Nucleation in Alloys

James A. Warren[1], Tamás Pusztai[2], László Környei[2], and László Gránásy[3]

[1]*Metallurgy Division, National Institute of Standards and Technology, Gaithersburg, Maryland 20899;*

[2]*Research Institute for Solid State Physics and Optics, P.O. Box 49, H-1525 Budapest, Hungary;*

[3]*Brunel Centre for Advanced Solidification Technology, Brunel University, Uxbridge, Middlesex, UB8 3PH, UK*

(Received …)

We extend the phase field model of heterogeneous crystal nucleation developed recently [L. Gránásy, T. Pusztai, D. Saylor, and J. A. Warren, Phys. Rev. Lett. **98**, 035703 (2007)] to binary alloys. Three approaches are considered to incorporate foreign walls of tunable wetting properties into phase field simulations: a continuum realization of the classical spherical cap model (called Model A herein), a non-classical approach (Model B) that leads to ordering of the liquid at the wall, and to the appearance of a surface spinodal, and a non-classical model (Model C) that allows for the appearance of local states at the wall that are accessible in the bulk phases only via thermal fluctuations. We illustrate the potential of the presented phase field methods for describing complex polycrystalline solidification morphologies including the shish-kebab structure, columnar to equiaxed transition, and front-particle interaction in binary alloys.

PACS number(s): 64.60.Qb, 64.70.Dv, 82.60.Nh

I. INTRODUCTION

When one cools a liquid below its melting temperature, it is no longer stable, and will freeze eventually [1]. However, the liquid will exist in a metastable state until a nucleation event occurs. In the study of nucleation, a distinction is made between *homogeneous* and *heterogeneous* nucleation [1,2]. Homogeneous nucleation occurs in an idealized pure material, where the only source of nucleation in an undercooled melt is due to fluctuation phenomena [1,2]. On the other hand, heterogeneous nucleation occurs in "impure" materials, where walls or some agent, usually particles substantially larger than the atomic scale introduced to the melt (either intentionally or not) facilitate nucleation by reducing the energy barrier to the formation of the stable phase. This reduction occurs when the impurities induce ordering in the liquid [3] that enhances the formation of the solid phase. Heterogeneous nucleation is not only a phenomenon of classic importance in materials science, but also remains one of continuously growing interest, due to the emerging technological interest in nano-patterning tech-

niques and control of related nano-scale processes [4]. In spite of its technological importance, heterogeneous nucleation is poorly understood due to difficulties in describing the interaction between the foreign matter and the solidifying melt.

In classical theory, the action of the impurity to enhance or suppress the solid phase can be formulated within the language of wetting. That is, given the surface energies for liquid-solid (γ_{SL}), wall-liquid (γ_{WL}), and wall-solid (γ_{WS}) boundaries, we may calculate the contact angle of a solid-liquid-wall triple junction (assuming isotropic surface energies [5]). Using Fig. 1 as a schematic guide (where the drop is imagined to be solid in liquid, not liquid in gas) to determine the contact angle ψ between the solid-liquid surface and the wall (with the angle subtending the solid material) we find a version of the Young-Laplace Equation:

$$\cos\psi = \frac{\gamma_{WL} - \gamma_{WS}}{\gamma_{SL}}. \qquad (1)$$

Clearly, within this framework, if $\psi = 0$ then the surface will be wet with the solid phase, and there will be no barrier to nucleation. In the case where $\psi = \pi$ the liquid phase is preferred at the interface, and the system behaves as if the particle were not there. Within the framework of the classical "spherical cap" model, the nucleation barrier is simply reduced by the catalytic potency factor $f(\psi)$ as follows, $W_{\text{hetero}} = W_{\text{homo}}\, f(\psi)$, where $f(\psi) = [\psi - \tfrac{1}{2}\sin(2\psi)]/\pi$ and $f(\psi) = \tfrac{1}{4}[2 - 3\cos(\psi) + \cos(\psi)^3]$ for two and three dimensions, respectively [1,5]. The above argument becomes more complex if the surface energies are anisotropic [5], but are not changed in qualitative detail.

Wetting of a foreign wall by fluids/crystals has been studied extensively [6] including such phenomena as critical wetting and phase transitions at interfaces [7]. Various methods have been applied to address these problems such as continuum models [8] and atomistic simulations [9]. Despite this inventory, recent studies [10] addressing heterogeneous crystal nucleation rely almost exclusively on the classical spherical cap model, which assumes mathematically sharp interfaces [1,11]. While this approach may quantitatively describe wetting on the macroscale, it loses its applicability [2,12] when the size of nuclei is comparable to the interface thickness (the nanometer range, according to experiment and atomistic simulations [13]). Such nanoscale nuclei are essentially "all interface". Recent investigations show [12] that the phase field approach (PFT, for recent reviews see [14,15]) can describe such non-classical nuclei. Indeed, the PFT can quantitatively predict the nucleation barrier for systems (e.g., hard-sphere, Lennard-Jones, ice-water, etc.) where the necessary input data are available [12,16]. We therefore adopt this approach to describe heterogeneous nucleation. Experimentally, the details of the wall-fluid interaction are embedded in more directly accessible quantities, such as the contact angle in equilibrium. It is thus desirable to develop a model that describes the wall in such phenomenological terms.

To address heterogeneous nucleation within the phase field approach, we need to include foreign walls. Ideally, we may regard the foreign "wall" as a new phase with all its chemical and wetting properties known. This is the case in previous stu-

dies addressing solidification in eutectic and peritectic systems, where the secondary crystalline phase appears via heterogeneous nucleation on the surface of the first-nucleated primary phase. Nucleation and subsequent growth on such *intrinsic walls* have been addressed in some depth in previous work [17].

More often, however, we do not have such detailed information on foreign walls, and have to satisfy ourselves with knowing only their wetting properties (e.g., the contact angle). It would be, therefore, desirable to work out PFT techniques for such cases. In order to distinguish this case from the fully characterized walls, and because of the fact that they can be represented in the PFT by boundary conditions, we are going to term them as *external walls*. Indeed, as we will see, to achieve this, we have to specify appropriate boundary conditions at the wall represented by a mathematical surface. Previous work along this line incorporates numerical approaches designed to ensure the desired contact angle [18], or either fixing the value of the phase field at the wall [19], or the normal component of the phase field gradient [15,19–22]. Early work in this area addressed only the non-wetting case ($\phi = 0$ corresponding to $\psi = \pi$) [19], or the semi-wetting case ($\psi = \pi/2$), realized by the no-flux boundary [15,19–21]. Recently, however, we have shown that either fixing the normal component of the phase field gradient (Model A) or the value of the phase field (Model B) appropriately at the wall, one can realize all kinds of contact angles [23].

It is appropriate to mention that ideas similar to those presented in our paper [23] seemed to be "in the air" in other branches of field theoretic modeling. For example, a simulation by Jacqmin [24] performed for a liquid-liquid interface forming contact angles of $\psi = \pm \pi/4$ with opposite walls suggests that he might have been aware of Model A, although neither a derivation of the model nor its general formulation valid for other contact angles has been presented in his paper. In fact, Model B has already been used in an earlier study [8(e)], however, for describing the wetting of solid surfaces by fluids, yet not for a structural order parameter. Finally, a few days before our prior paper on this topic [25] has been published electronically, a similar work has been submitted, which outlines Model A for interfaces between two fluids. These techniques have been worked out for single fields, and they have yet to be generalized to cases where the structural order parameter is coupled to other fields.

Herein, we generalize the approaches described in [23] for the solidification of binary alloys (structural order parameter coupled to a concentration field). It will be shown that with a specific parabolic approximation of the free energy surface the contact angle vs. boundary condition relationships described in [23] remain valid. After developing the model for isotropic, binary alloys, we extend the model (adding noise, grain boundary effects and interfacial anisotropy) allowing us to perform simulations of heterogeneous nucleation during the growth of a polycrystalline material.

II. PHASE FIELD THEORY FOR WETTING AND HETEROGENEOUS NUCLEATION

Recently, a rich array of phenomena has been modeled using a phase field theoretic approach that has a fairly simple form (see the appendices of [15]):

$$F = \int dV \left[f(\phi, c) + \frac{\varepsilon^2}{2} \boldsymbol{\Gamma}^2(\nabla\phi \cdot \boldsymbol{R}) + f_{ori}(\nabla \boldsymbol{R}) \right], \tag{2}$$

where $f(\phi,c)$ has the form of a skewed double well, with minima in the two phases at $\phi = 0$ (liquid) and $\phi = 1$ (solid), and the difference in height being controlled by the thermodynamic variables such as temperature T and concentration c. In this model T is assumed uniform. The gradient coefficient, ε, sets the interface width, while the form of Γ, a homogeneous degree one function of its argument, determines the anisotropy. The contribution from orientation due to grain boundaries is embedded in the local orientation matrix $\boldsymbol{R}$. In general, $\boldsymbol{R}$ is an $SO(3)$ object, and thus transforms in manner consistent with this group. There are a number of equivalent representations of $\boldsymbol{R}$ [26, 27], but here we will use a quaternion form from [28]. $\nabla\phi \cdot \boldsymbol{R}$ rotates the vector $\nabla\phi$ into the frame of the orientation of the crystal. The function then Γ determines the penalty for gradients in this direction. It thus represents the local interface energy anisotropy. As a homogeneous degree one function, $\boldsymbol{\Gamma}(\mathbf{v})$ can be written as

$$\boldsymbol{\Gamma}(\mathbf{v}) = |\mathbf{v}| \, (1 + \beta(\mathbf{n})),$$

where $\mathbf{n} = \mathbf{v}/|\mathbf{v}|$, is the normal to the level sets of ϕ, in the coordinate system of the crystal, and thus is the natural extension of the surface normal in classical theory to a phase field model, and β is necessarily a homogeneous degree zero function of its argument. For four-fold symmetry, a common choice for $\beta = \alpha (n_x^4 + n_y^4 + n_z^4)$, where α is a constant. When $\boldsymbol{\Gamma}(\nabla\phi) = |\nabla\phi|$ (or $\beta = 0$), the interface energy will be independent of the orientation of the phase boundary. Finally the orientation penalty taken to have the simple form

$$f_{\text{ori}} = HTu(\phi) \, |\nabla \boldsymbol{R}| + O(|\nabla \boldsymbol{R}|^2),$$

where we use the standard L^2 norm of the gradient of the orientation, which is a metric that yields the local misorientation. The function $u(\phi)$ is zero in the liquid, and increases in the solid, where grain boundary energies are well defined. In quaternion notation

$$|\nabla \boldsymbol{R}| = \left(\sum_i (\nabla q_i)^2 \right)^{1/2}$$

[26, 28].

Until we return to the more complex case of polycrystalline growth later in the manuscript, we will focus on the isotropic case. We thus drop f_{ori} and assume $\mathbf{\Gamma}(\mathbf{v}) = |\mathbf{v}|$, yielding a standard model phase field model of a binary alloy, like that found in Warren and Boettinger [29] and many others [30], with the form

$$F = \int dV \left[f(\phi, c) + \frac{\varepsilon^2}{2} |\nabla \phi|^2 \right]. \tag{3}$$

Equations of motion then have the form

$$\frac{\partial \phi}{\partial t} = -M_\phi \frac{\delta F}{\delta \phi} = M_\phi \left[\varepsilon^2 \nabla^2 \phi - \frac{\partial f}{\partial \phi} \right], \tag{4}$$

$$\frac{\partial c}{\partial t} = \nabla \cdot M_c \nabla \frac{\delta F}{\delta c} = \nabla \cdot M_c \nabla \frac{\partial f}{\partial c}, \tag{5}$$

where M_ϕ and M_c are mobilities.

As in classical theory, the critical fluctuation (nucleus) represents an extremum of the free energy. Thus it can be found by solving the appropriate Euler-Lagrange equations. Mass conservation needs to be taken into account here, a constraint that can be enforced by adding $\Lambda \int c(\mathbf{r})\, \mathrm{d}V$ to the free energy, where Λ is a Lagrange multiplier

$$\frac{\delta F'}{\delta \phi} = 0, \tag{6}$$

$$\frac{\delta F'}{\delta c} = 0, \tag{7}$$

where $F' = F + \Lambda \int c(\mathbf{r})\, \mathrm{d}V$ is the free energy functional that includes the term with the Lagrange multiplier.

We wish now to supplement this model in a manner that will allow for a physical representation of the influence of a new material on the statics and dynamics of crystallization. There are several ways that this can be done: (i) the imposition of appropriate boundary conditions on the above equations, or (ii) the addition to the model of a second phase field to directly model the impurities. Both of these approaches will allow us to to model the wetting of a chemically inert phase embedded in the solid-liquid matrix, and concomitantly, develop a physical model of heterogeneous nucleation. Having developed these two approaches, and examining their respective benefits and costs, we will then discuss their relationship to the ''full'' three-phase-field model, and demonstrate the common mathematical basis for all of models developed herein. We now present, in substantial detail, the specifics of these assertions, and then use the model to examine several relevant examples.

A. Defining "external" walls

There are several mathematical approaches to modeling a three phase system. The first we consider involves treating the inert material as a sharp wall, the walls influence is controlled by the behavior of the alloy abutting the wall. The two most natural choices to consider are either specifying $\nabla\phi \cdot \mathbf{n}$ or ϕ on the boundary. We explore both below.

In steady state the one dimensional equations describing the system can be integrated to find

$$\frac{\varepsilon^2}{2}\left(\frac{\partial\phi}{\partial x}\right)^2 = \Delta f(\phi,c) = f(\phi,c) - \mu(c - c_\infty) - f_\infty ;$$

$$\text{const.} \equiv \mu = \frac{\partial f}{\partial c} \quad , \tag{8}$$

where μ is the chemical potential, $f_\infty = f(\phi_\infty, c_\infty)$ and ϕ_∞ and c_∞ are the far field values of ϕ and c respectively.

From Eqs. (8) we see immediately that specifying the value of either ϕ, $\partial f/\partial x$ or c at the boundary immediately determines the other two (in steady state). In this manuscript we will examine the consequences of three possible choices (i) specification of ϕ at the boundary (ii) specification of a normal gradient $\nabla\phi\cdot\mathbf{n}$ at the boundary ($\mathbf{n}$ is the surface normal), and finally (iii) introduction of a new bulk field term ϕ_W, an auxiliary field that takes the value 1 in the wall material (where ϕ = 0). We explore this last approach in a subsequent section, as it will become the foundation for implementing all of the methods described herein.

We follow the ideas of Cahn [7], who examined the problem of introducing a wettable interface into a binary alloy liquid with a miscibility gap (the system therefore had a critical point). Cahn imposed an "interface function" that determined a boundary condition on the concentration field, and then examined the behavior of the system near the critical point. We now propose to do the same analysis in the context of the *non-conserved* phase field model of an ideal binary solution. We should note that the use of a *structural* order parameter in this analysis has specific physical implications that are non-trivially different from those realized under Cahn's analysis of a *conserved* order parameter. In particular, as the dynamics these two types of flows is substantially different, we expect the behavior of nucleation in these systems to be qualitatively different. The analysis of equilibrium, will, however, be quite analogous, and we will adapt considerable material developed by others for our own use.

We assume a free energy of the following form, where there is a boundary S, which specified the presence of an "inert" wall.

$$F = \int_S Z(\phi)dS + \int dV\left[f(\phi,c) + \frac{\varepsilon^2}{2}\boldsymbol{\Gamma}^2(\nabla\phi)\right]. \tag{9}$$

Minimization of the total free energy $\delta F = 0$ yields both Eqs. (4) and (5) as well as the boundary condition

$$\delta\phi\,[z(\phi) + \varepsilon^2\nabla\phi\cdot\mathbf{n}] = 0 \quad \text{on } S, \tag{10}$$

where $\mathbf{n}$ is the outward pointing normal to the surface S and $z(\phi) \equiv \partial Z/\partial\phi$. This boundary condition can be met in one of two ways, either $-\varepsilon^2\nabla\phi\cdot\mathbf{n} = z(\phi)$ (Model A) or $\phi = \text{const.}$ (Model B), on the boundary. These names follow the nomenclature of Ref. 23, but we will allow for another way of setting the normal component of the phase field gradient at the interface (Model C). For concreteness we will explore herein both the model found in Ref. 23, where a special choice for $z(\phi)$is used, namely that along the inert boundary, all phase field contours have the same form as the one-dimensional profile rotated by an angle ϕ, as well as a simple quadratic model, where $Z = 6\gamma_{SL}\,(\tfrac{1}{2}g\phi^2 + h\phi)$, with g and h specified constants. Specifically we have for Models A and C on surface S:

Model A:

$$z = -\varepsilon^2(\nabla\phi\cdot\mathbf{n}) = -\,6\gamma_{SL}\,\phi(1-\phi)\cos(\psi), \tag{11}$$

Model B:

$$\phi = \text{const.} \tag{12}$$

Model C:

$$z = -\varepsilon^2(\nabla\phi\cdot\mathbf{n}) = 6\gamma_{SL}\,(g\phi + h), \tag{13}$$

where ψ is the imposed contact angle, and the specific choice of $z(\phi)$ in Model A will become self-evident after f is specified in a subsequent section of this manuscript. Models A, B, and C are all legitimate solutions to the variational problem, but may have different consequences on the dynamics of the system. Note that if there are multiple interfaces, then the boundary condition applies at each instance of the surface with in or surrounding the alloy. We see that the boundary condition generally relates ϕ to $(\nabla\phi\cdot\mathbf{n})$ on surface S.

Next, we briefly deduce Models A, B, and C. Along these lines, we demonstrate that, under certain circumstances, a three-phase-field model (liquid-solid-wall) can be reduced to a single phase field model with a boundary condition $\phi = \phi_0 = \text{const.}$ at the inert interfaces (Model B) and show that how Model A can be nested into a three-phase-field model.

B. Derivation of Model A

We wish to ensure in equilibrium that the solid-liquid interface has a fixed contact angle ψ with a foreign wall placed at $z = 0$. To achieve this, we prescribe the following boundary condition at the wall, which can be viewed as a binary generalization of Model A presented in Ref. 23:

$$(\mathbf{n}\cdot\nabla\phi) = \left(\frac{2\Delta f[\phi, c(\phi)]}{\varepsilon^2}\right)^{1/2}\cos(\psi)\,. \tag{14}$$

The motivation for this boundary condition is straightforward in the case of a stable triple junction, in which the equilibrium planar solid-liquid interface has a contact angle ψ with the wall. The wall is assumed to lead to an ordering of the adjacent liquid, an effect that extends into a liquid layer of thickness d, which is only a few molecular diameters thick (see e.g., [31,32]). If we take a plane $z = z_0$, which is slightly above this layer, i.e., $z_0 > d$, on this plane, the structure of the equilibrium solid-liquid interface remains unperturbed by the wall. Then, at $z = z_0$ the phase field and concentration profiles are trivially related to the equilibrium profiles across the solid-liquid interface via the integral form of the EL equation that holds only for the planar interface:

$$\frac{\varepsilon^2}{2}\left(\frac{\partial\phi}{\partial n_{SL}}\right)^2 = \Delta f[\phi, c(\phi)], \tag{15}$$

where n_{SL} is a spatial coordinate normal to the solid-liquid interface, while the component of $\nabla\phi$ normal to the wall is then $(\mathbf{n}\cdot\nabla\phi) = (\partial\phi/\partial n_{SL})\cdot\cos(\psi) = (2\Delta f/\varepsilon^2)^{1/2}\cdot\cos(\psi)$. Remarkably, if the parabolic groove approximation by Folch and Plapp [33] is applied for the free energy surface, one finds that conveniently $\Delta f[\phi,c(\phi)] \propto \phi^2(1-\phi)^2$.

C. Three-phase model vs. Model B

Typically to model three phases (solid, liquid and wall), we would introduce three phase field variables (ϕ_S, ϕ_L, and ϕ_W, respectively), where each variable takes on the value 1 in its named phase and 0 elsewhere, and impose the constraint that

$$\phi_S + \phi_L + \phi_W = 1. \tag{16}$$

This constraint requires that phases evolve only by transforming into another phase (no holes can develop). The constraint reduces the problem to only two independent phase field variables. For specificity, we will assume a liquid/solid binary alloy system at a uniform temperature (similar to the one employed by Warren and Boettinger [29] and many others [30]). We then postulate a free energy of the following form

$$F = \int dV \left[f(\phi_S, \phi_L, \phi_W, c) + \kappa_S \left|\nabla \phi_S\right|^2 + \kappa_L \left|\nabla \phi_L\right|^2 + \kappa_W \left|\nabla \phi_W\right|^2 \right], \tag{17}$$

where f is a local free energy density with minima at $\phi_j = 0,1$ for all three phases $j = L,S,W$. The stability or metastability of each of these minima is dependent on the particulars of the form of f, which is in turn dependent upon the thermodynamic particulars of the alloy in question. We will specify a particular choice of f below. The gradient terms have a form that yields an isotropic interface energy, a choice which can be remedied in a number of ways, but this choice in no way effects the gist of the argument below. Using the constraint Eq. (16), we can eliminate one of the variables (in this case we will choose the liquid), re-label the solid variable $\phi_S \to \phi$ and obtain

$$F = \int dV \left[f(\phi, \phi_W, c) + (\kappa_S + \kappa_L) \left|\nabla \phi\right|^2 + 2\kappa_L \nabla \phi \cdot \nabla \phi_W + (\kappa_W + \kappa_L) \left|\nabla \phi_W\right|^2 \right]. \tag{18}$$

In a typical phase field treatment, at this stage we would minimize the free energy with respect to our two remaining phase field variables, and postulate dynamics according to a law of gradient flow. However, in this instance we take a different approach, namely that the profile of ϕ_W is *determined by the free energy in steady state* and it is comprised of a series of *sharp* jumps between regions where $\phi_W = 1$ (inert wall) and $\phi_W = 0$ (liquid or solid). In principle, this implies some singular behavior for the total free energy density, if it is to yield a sharp interface in ϕ_W (and therefore discontinuous jumps in the other variables). However, as we demonstrate below, the particular nature of these singularities is irrelevant for practical computations. Given this constraint, we write the dynamical equations as

$$\frac{\partial \phi}{\partial t} = -M_\phi \frac{\delta F}{\delta \phi} = -M_\phi \left[\frac{\partial f}{\partial \phi} - 2(\kappa_S + \kappa_L)\nabla^2 \phi - 2\kappa_L \nabla^2 \phi_W \right], \tag{19}$$

$$\frac{\partial c}{\partial t} = \nabla \cdot M_c \nabla \frac{\delta F}{\delta c} = \nabla \cdot M_c \nabla \frac{\partial f}{\partial c}. \tag{20}$$

Note that the form of Eq. (19) is, excepting the term proportional to $\nabla^2 \phi_W$, identical to Eq. (4).

We assume that ϕ_W is time independent, and makes discontinuous jumps between regions of inert wall ($\phi_W = 1$) and the regions of liquid or solid ($\phi_W = 0$). As $\phi = 0$ in regions where $\phi_W = 1$, it is clear that ϕ must make discontinuous jumps that mirror ϕ_W. Given this, we assume the existence of an auxiliary function $\phi_R(x, t)$ and write

$$\phi = \phi_R(x, t)\,[1 - \phi_W(x, t)], \tag{21}$$

where $\phi_R(x, t)$ is differentiable everywhere ($\mathcal{C}^1$) and $\phi_R(x, t) = \phi_0$ at the inert wall. If we insert these expressions into Eq. (19), and equate orders in the divergences associated with spatial derivatives in ϕ_W, we find that at the wall

$$\phi_0 = \frac{\kappa_L}{\kappa_S + \kappa_L}, \tag{22}$$

for all time. Note that the value of ϕ_0 is *independent of far field boundary conditions*.

Thus, we see that these equations effectively yield a *boundary condition* on $\phi = \phi_0$ (Model B) at inert particle interfaces. Hence, we propose that an essentially equivalent approach the above problem is to simply *impose* this boundary condition, and drop the additional equations associated with the other phase fields. Either method will be equally effective, however implementation may be easier for one or the other method depending on the particulars of the problem to be considered.

D. Three-phase model vs. Model A

In addition to allowing the solution to Model B, the auxiliary field ϕ_W is a useful numerical convenience for implementing the classical approach described above in the previous section for Model A. Specifically, we can extend the integrals over the inert wall and the containing volume to all of space (the space containing both the liquid/solid and the wall material) by the following modifications to

$$F = \int dV \left[Z(\phi)|\nabla\phi_W| + \left(f(\phi, c) + \frac{\varepsilon^2}{2}\boldsymbol{\Gamma}^2(\nabla\phi) \right)(1-\phi_W) \right], \tag{23}$$

where $|\nabla\phi_W|$ is a Dirac δ-function that locates $Z(\phi)$ to the interface, while the new factor $(1 - \phi_W)$ locates the free energy density for the liquid/solid phase to those regions where $\phi_W = 0$. Computing δF yields a modified equation for ϕ, specifically,

$$-\frac{1}{M_\phi}\frac{\partial\phi}{\partial t} = \frac{\delta F}{\delta\phi} = \left(\frac{\partial f}{\partial\phi} - \varepsilon^2\nabla^2\phi \right)(1-\phi_W) + \left[z(\phi) + \varepsilon^2\nabla\phi\cdot\mathbf{n} \right]|\nabla\phi_W|, \tag{24}$$

where we have used $\mathbf{n} = \nabla\phi_W/|\nabla\phi_W|$. This expression is in some sense "obvious", since all we are doing is adding the Model A boundary condition multiplied by a δ-function to the original variation over the volume bounded by the inert wall. Thus, be prescribing the auxiliary field ϕ_W, we may perform computations over all of space, and need not explicitly impose boundary conditions on the liquid-solid material at the inert wall.

E. A comment on grain boundaries

At this juncture it is useful to briefly consider the grain boundary model mentioned in the previous section, as there is a mathematical analogy between the introduction of the boundary condition in the phase field model through $|\nabla\phi_W|$ and the grain boundary energy penalty term $|\nabla R|$. As first noticed by Tang *et al.* [34], this grain boundary model is mathematically

identical to the model of Cahn for critical wetting. Now, with the above analysis, the reasons for this mathematical equivalence become obvious. Specifically, if R has a step discontinuity at a point in space, a term of the form

$$\int_V u(\phi)\left|\nabla R\right| dV = \Delta\theta \int_S u(\phi) dS \,,$$

where $\Delta\theta$ is the misorientation across the grain boundary. Thus, the model including grain boundary effects described above, and solved in subsequent sections, includes two effective boundary-like terms, one static (the inert particles described by ϕ_W), and one dynamic (the grain boundaries, described by $R(q)$.

F. Physical interpretation of Models A, B, and C

At this stage, it is appropriate discuss the physical pictures underlying Models A, B, and C.

Model A places the mathematical surface at which the boundary condition acts slightly beyond the boundary layer influenced by the wall. Thus the bulk liquid and solid phases in contact with the wall are connected through an unperturbed solid-liquid interface profile, and the derivation of the interface function for the desired contact angle is straightforward. All effects of liquid ordering and solid disordering due to the wall are buried into the contact angle (realized by the particular surface function) as in the classical sharp interface model. Then, the total free energy of the system incorporates both a volumetric and a surface contribution. Model B prescribes liquid ordering and solid disordering at the wall explicitly. A shortcoming is though that it implicitly assumes that the wall enforces the formation of *a specific layer of the solid-liquid interface* (corresponding to ϕ_0), simplifying considerably the nature of the wall-liquid / wall-solid interactions. Here, the free energy of the system originates exclusively from the volumetric contribution.

Relying on a model parameter (h) of less straightforward physical interpretation than either the contact angle or the value of ϕ_0, Model C is able to prescribe local conditions that are not present inside the solid-liquid interface. For example, ϕ values may appear along the wall that fall outside of the (0, 1) range. Note that the appearance of such states is not unnatural: they are also present in phase field models, when Langevin noise is added to the equations of motion. These values of ϕ may be viewed, as local states that are either more ordered or disordered than the bulk crystal and liquid phases (e.g., for $\phi > 1$, atoms are more localized that in the bulk solid; while $\phi < 0$ might indicate a liquid with density deficit). Further work is, however, desirable that relates the model parameters to microscopic properties (such as molecular interaction / molecular scale misfit at the wall). Remarkably, Model C incorporates *both structural change at the interface and a surface function*, both of which contribute to the total free energy of the system. In this respect, Model C can be viewed as a generalization of the other two models. Nevertheless, we note that generally Model A cannot be obtained as a limiting case of Model C. It is remarkable, however, that setting $g = h = 0$ in Model C, one can recover Castro's approach that uses the "no-flux" boundary

condition [$(\mathbf{n}\cdot\nabla\phi) = 0$] to realize a 90° contact angle [20]. This specific case can also be recovered in Model A by prescribing $\psi = 90^{o}$. In these specific limits, solutions of Models A and C coincide.

III. MATERIALS PROPERTIES

In this work we employ a parabolic well approximation to the free energy density based on the work of Folch and Plapp [33] (FP free energy henceforth). Specifically, we select $f(\phi, c)$ to be appropriate for an ideal solution

$$f(\phi,c) = wG(\phi) + X\left\{\tfrac{1}{2}(c-\bar{c}-\Delta c(T)[1-p(\phi)])^2 + [c_S(T)-\bar{c}]\Delta c(T)[1-p(\phi)]\right\}, \tag{25}$$

where $G(\phi) = \phi^2(1-\phi)^2$ is a double-well with minima at $\phi = 0, 1$ (the common "ϕ^4-potential"), w is the scale of the height of the double well, X is an energy scale associated with chemical changes in the system, and $p(\phi) = \phi^3(10 - 15\phi + 6\phi^2)$ is an interpolating function between phases with

$p(0) = 0$ and $p(1) = 1$. The functions $c_L(T)$ and $c_S(T)$, which determine $\Delta c(T) = c_L - c_S$ are the concentrations of liquid / solid coexistence (the liquidus and solidus), which in turn depend on the temperature, T, (which has been assumed uniform). Finally, $\bar{c}$ is a concentration locating the minima in the solid free energy. This free energy model has the advantage of reproducing a variety of phase diagrams, while allowing for a significant amount of analysis in one dimension, as will discussed below. This parabolic well approximation to the free energy surface has, furthermore, the interesting property that $\Delta f[\phi, c(\phi)] = wG(\phi)$, where $c = c(\phi)$ is the explicit relationship between c and ϕ emerging from the Euler-Lagrange equation [Eq. (7)] for the concentration field [35]. This feature means that in equilibrium (whether stable or unstable, i.e., planar surface or nuclei) there is no chemical contribution to the free energy. This also means that a single solution of the EL equation for the one--component case can be transformed into an infinite number of binary solutions using the explicit relationships $c = c(\phi)$ emerging from Eq. (7), provided that the latter does not contain a $\nabla^2 c$ term. {We note that for nuclei the $c = c(\phi)$ relationship depends on the initial composition of the liquid [13].} Since these features simplify the analytical calculations considerably, we use the approximate thermodynamics given by Eq. (25) throughout this work. We note, however, that in general $\Delta f[\phi, c(\phi)]$ has a more complex form.

In order to do numerical calculations, we need to specify a number of parameters in the theory. ε, X, w, $c_L(T)$, $c_S(T)$, and T, and for dynamics, the mobilities M_ϕ and M_c. Herein, these model parameters are chosen so that our computations are comparable to the Cu-Ni ideal solution applied in many earlier studies [15,21,29,36]. With this in mind, we choose a temperature $T = 1574$ K, where $c_S = 0.399112$, and $c_S = 0.466219$, and $X = 7.0546\times10^9$ J/m^3.

Next, we chose the interfacial parameters: In the case of nucleation studies relying on solving the EL equations, we have used $d_{10\text{-}90\%} = 1$ nm for the 10%-90% interface thickness, as expected on the basis of atomistic simulations [13, 14]. The in-

terfacial free energy has been chosen as the average (γ_{SL} = 0.2958 J/m^2) of the experimental values for Cu (0.223 and 0.232 J/m^2) and Ni (0.364 J/m^2) from the grain boundary groove and dihedral techniques (data compiled in [37]). Accordingly, $\varepsilon^2 = 3\gamma_{SL}d_0 = 4.038\times10^{-10}$ J/m and $w = 6\gamma_{SL}/d_0 = 3.899\times10^9$ J/m^3, where $d_0 = d_{10\text{-}90\%}/\ln(0.9/0.1)$. These calculations can be regarded quantitative.

As our illustrative computations for complex structures forming via heterogeneous nucleation are intended to be merely technology demonstrators, we aimed at only qualitative modeling.

For example, in describing the shish-kebab morphology appearing in polymer-carbon nano-tube systems [38], we have used an ideal solution approximant of the Cu-Ni alloys, applied in several previous works of us [21,36]. However, to mimic polymers, a high anisotropy of six-fold symmetry for the kinetic coefficient [see Fig. 2(a)] has been applied

$$\frac{M_\phi}{M_{\phi,0}} = \left\{1-3\varepsilon+\varepsilon\frac{4\eta^2\phi_z^4+(\phi_x^2+\phi_y^2)^2\{3+\cos[6\cdot\mathrm{atan}(\phi_y/\phi_x)]\}}{\left(\phi_x^2+\phi_y^2+\phi_z^2\right)^2}\right\},$$

($\varepsilon = {}^1/_3$ and η = 0.001), a combination that mimics the behavior of polymeric systems in that the asymptotic growth form (kinetic Wulff shape, calculated according to Ref. 39) is a hexagonal plate [see Fig. 2(b)]. [Here we use the notation $(\nabla\phi)^2 = \phi_x^2 + \phi_y^2 + \phi_z^2$.] In the simulations, we have used the following parameter set for the free energy: $\varepsilon^2 = 1.65\times10^{-8}$ J/m, w = 5.2810^7 J/m^3, while X is the same as above, and assuming that the diffusion coefficients in the liquid and solid are $D_l = 10^{-9}$ m^2/s and D_s = 0, respectively, while the phase field mobility is M_ϕ = 0.05 m^3/(J·s).

Other simulations for solidification in the presence of foreign particles have been performed for a 10% - 90 % interface thickness of 5 nm, and a slightly higher interfacial free energy (0.360 J/m^2). The respective values for the model parameters are: $\varepsilon^2 = 4.95\times10^{-9}$ J/m, and $w = 3.96\times10^8$ J/m^3.

Finally, a few illustrative computations have been performed to model the columnar to equiaxed transition as a function of contact angle in the $Al_{55}Ti_{45}$ alloy. The thermodynamic properties have been taken from a CALPHAD-type assessment of the phase diagram [40]. For further details see Ref. 41. Here, the same anisotropy function has been used for M_ϕ as in the case of the polymeric system, however, now with ε = 0.3 and η = 1.0. The respective orientation dependence of M_ϕ and the respective asymptotic growth form (octahedron) are shown in Fig. 3.

IV. RESULTS AND DISCUSSION

Before performing numerical solutions to the equations it is useful to determine those cases where analytic calculations are tractable. With this is mind we examine threes cases of interest in steady state: (i) a triple junction (solid-liquid-wall) of

3 flat interfaces, (ii) an undercooled liquid in contact with and inert wall (iii) solid droplet (spherical-cap) in contact with an inert wall.

A. Wetting properties of external walls

In order to compare these phase field models with Young's Equation [Eq. (1)], we must compute the surface energies and other relevant quantities. The surface energies can be computed using the first integral and arguments found in a number of sources [8, 41]. In general the surface energy between any two, semi-infinite phases *A* and *B* will be

$$\gamma_{AB} = 2\int_{-\infty}^{\infty} dx \Delta f[\phi, c(\phi)]\,. \tag{26}$$

We are going to address wetting properties using this expression valid for far field behavior, and utilizing the specific form of the free energy surface given by Eq. (25).

1. The triple junction of 3 flat interfaces

In order to examine all of these cases, it is useful to consider flat interfaces in equilibrium. The three phases will coexist at the melting point. Utilizing the properties of the FP free energy, the liquid/solid interface free energy γ_{SL} far from the junction is

$$\gamma_{SL} = \varepsilon\int_0^1 d\phi\sqrt{2\Delta f[\phi, c(\phi)]} = \varepsilon\sqrt{2w}\int_0^1 \phi(1-\phi)d\phi = \frac{\varepsilon\sqrt{2w}}{6} \tag{27}$$

Regardless of whether we impose a condition on ϕ or $\nabla\phi\cdot\mathbf{n}$, the interface boundary condition establishes a value for ϕ. As discussed above, ϕ is either specified ($\delta\phi = 0$ on the boundary), or, if an interface function is specified than we may combine Eq. (8) with the interface boundary condition to find the roots of

$$2\varepsilon^2\Delta f[\phi, c(\phi)] = (6\gamma_{SL})^2\, G(\phi) = z^2(\phi), \tag{28}$$

which has the simpler form

$$6\gamma_{SL}\,\phi\,(1-\phi) = \pm\, z(\phi), \tag{29}$$

Eq. (28), combined with $\partial f/\partial c = \mu$, is sufficient to determine the interface values of ϕ and c. In general, these expressions will have multiple roots, and the system's selection of a particular root will be determined such that the free energy is minimized. We denote the roots selected when either liquid or solid abuts the inert wall as ϕ_L and ϕ_S respectively.

Given ϕ at the wall, we may determine the energies of wall-liquid and wall-solid boundaries as

$$\gamma_{WL} = Z(\phi_L) + \gamma_{SL}[3\phi_L^2 - 2\phi_L^3], \tag{30}$$

$$\gamma_{WS} = Z(\phi_S) + \gamma_{SL}[1 - 3\phi_S^2 + 2\phi_S^3]. \tag{31}$$

Thus the expression for the contact angle reads as

$$\cos(\psi) = \frac{Z(\phi_L) - Z(\phi_S)}{\gamma_{SL}} + (3\phi_L^2 - 2\phi_L^3) - \left[1 - 3\phi_S^2 + 2\phi_S^3\right]. \tag{32}$$

This expression includes the mild assumption that the free energies of flat, isolated interface can be used in constructing a Young's equation. While this is exact for the stable triple junction in an infinite system, it is only an approximation in the undercooled state, as all the field variables interact in the triple junction region, but the approximation may hold under a variety of circumstances. We will test the accuracy of this through simulations shown below.

For Model A, the above analysis is nearly trivial, as $\phi_{WL} = 0$, $\phi_{WS} = 1$, and the contact angle is actually the control parameter of the model. Accordingly, the surface function can be expressed as $Z(\phi) - \gamma_{WL} = \gamma_{SL}\cos(\psi)[2\phi^3 - 3\phi^2] = (\gamma_{WS} - \gamma_{WL})[2\phi^3 - 3\phi^2]$, yielding 0 for the bulk liquid phase ($\phi = 0$), and $(\gamma_{WS} - \gamma_{WL})$ for the bulk solid ($\phi = 1$) phase at the interface.

For the case, when ϕ is specified at the interface (Model B) then $\phi_L = \phi_S = \phi_0$ and the expression for the contact angle simplifies to $\cos(\psi) = 2\phi_0^2(3 - 2\phi_0) - 1$. In this case we see that as ϕ_0 ranges from 0 to 1 then ψ ranges from 0 (total liquid wetting, solid dewetting) to π (total solid wetting, liquid dewetting). This is not surprising, since making the interface "solid-like" causes solid to wet the surface, while when the surface is "liquid-like" the reverse is true.

For Model C, things are a bit more complicated (not surprisingly), but the analysis is revealing. We have at the boundary that $\phi(1-\phi) = \pm(h + g\phi)$, which can be quickly solved to find up to four real roots

$$\begin{aligned} \phi_{1,2} &= \frac{1}{2}\left[1 - g \pm \sqrt{(1-g)^2 - 4h}\right], \\ \phi_{3,4} &= \frac{1}{2}\left[1 + g \pm \sqrt{(1-g)^2 + 4h}\right]. \end{aligned} \tag{33}$$

It simplifies the analysis of these roots to consider the case $g = 0$, as this assumption does not change the character of the solutions, only the particulars. (Note that this case, $(\mathbf{n}\cdot\nabla\phi) = -$ const., which can be viewed as a straightforward generalization of Castro's "no-flux" condition for establishing a contact angle of $\pi/2$ [20].) In this case, one finds that the minimum free energy solutions for ϕ are

$$\phi_S = \frac{1}{2}\left[1+\sqrt{1-4h}\right],$$
$$\phi_L = \frac{1}{2}\left[1-\sqrt{1+4h}\right], \tag{34}$$

where we note that ϕ will take values *outside* the range [0,1] at the wall. As ϕ is a structural order parameter, and not a concentration, this is not, necessarily, unphysical as we mentioned above. This changes some of the signs for some of the terms in the expression for the surface energy, and care must be taken. Using these values of ϕ_0, we can calculate the contact angle to be

$$\cos\psi = \frac{1}{2}\left[(1-4h)^{3/2} - (1+4h)^{3/2}\right]. \tag{35}$$

Note that if $h > ¼\,[2\cdot 3^{1/2} - 3]^{1/2} \approx 0.1703$, then the contact angle is π (complete wetting by the liquid), while if $h < -¼\,[2\cdot 3^{1/2} - 3]^{1/2} \approx -0.1703$ the contact angle is 0 and the solid "wets" the interface. A plot of the contact angle as a function of h is given in Fig. 4.

2. Undercooled liquid next to an inert wall, and "critical" wetting: 1D solutions

In this sub-section, we consider a semi-infinite supersaturated (undercooled) liquid [$c_\infty \neq c_L(T)$, $\phi_\infty = 0$] in contact with a planar wall placed at $z = 0$. Then the first integral of the respective 1D Euler-Lagrange equation for the phase field reads as

$$\frac{\varepsilon^2}{2}\left(\frac{\partial\phi}{\partial z}\right)^2 = f - f_\infty - \mu(c - c_\infty) = wG(\phi) - X\Delta c(c_L - c_\infty)\,p(\phi) = \Delta f[\phi, c(\phi)]. \tag{36}$$

Here, the FP choice of the free energy density yields a skewed double well as a function of ϕ.

Model A shows a classical behavior: neither liquid ordering nor critical wetting is predicted at the interface.

In Model B liquid ordering is inherent and a spinodal-like behavior can be seen at high enough driving force. Here, we have ϕ_0 = const. $\in$ [0, 1] at the wall. Under such conditions, the 1D Euler-Lagrange equation can be integrated to obtain $\phi(x)$, yielding a solution representing a metastable equilibrium (supersaturated liquid in contact with the wall). Remarkably, Eq. (36) can only be integrated to yield a real solution in the region, where $wG(\phi) - X\Delta c(c_L - c_\infty)p(\phi) \geq 0$. For $wG(\phi) - X\Delta c(c_L - c_\infty)p(\phi) < 0$, only a time dependent solution exists: a propagating solidification front. The critical supersaturation that separates these two types of solutions, while prescribing a fixed ϕ_0 value at the wall, is given by the condition $wG(\phi_0) - X\Delta c(c_L - c_\infty)p(\phi_0) = 0$, yielding $S_{crit} = wG(\phi)/[X\Delta c^2 p(\phi)]$. (It is the binary analogue of the critical undercooling of the unary systems discussed in Ref. 23.) The critical supersaturation vs ϕ_0 relationship corresponding to the FP parameters specified in

Section III is shown in Fig. 5. It can also be shown (see next subsection) that the nucleation barrier, the solid phase has to pass to start solidification, tends to zero in this limit, and the solid phase wets ideally the wall. This phenomenon is analogous to the critical wetting of a solid wall seen in two-fluid systems near the critical point. However, we have here a solid and a liquid phase, instead of the two fluids.

For $g = h = 0$, Model C coincides with Model A at $\psi = \pi/2$, therefore, under such conditions no surface ordering/disordering or spinodal are observed. Despite surface ordering/disordering, for $h > 0$, no surface spinodal exists in Model C ($g = 0$). However, for $h < 0$, where $\phi \in [0, 1]$ at the wall, Model C ($g = 0$) predicts both surface ordering and a spinodal. The relationship between h and the critical supersaturation can be computed using the expressions $S_{crit} = wG'(\phi)/[X\Delta c^2 p'(\phi)]$ and $h = \chi(\phi) = -\{G(\phi) - p(\phi)X\Delta c(c_L - c_{crit})/w\}^{1/2}$, where $c_{crit} = c_L - S_{crit}\Delta c$, where the expression for S_{crit} originates from the condition that the critical state corresponds to the extremum of the loop in $\chi(\phi)$ that incorporates the point $\phi = 0$, $\chi = 0$. (Note that the expression for S_{crit} is the condition both for the maximum gradient $\partial\phi/\partial z$ of the 1D solution and for the location of the central hill of the double-well free energy.) The respective S_{crit} vs. $-h$ relationship is shown for the Cu-Ni system with $d_{10\text{-}90\%} = 1$ nm interface thickness at $T = 1574$ K in Fig. 6. We note that with the actual choice of the model parameters (as for other continuum models), the spinodal point between the solid and supersaturated liquid falls into the physically inaccessible region of negative concentrations (see the discussion later).

B. Heterogeneous nucleation on external walls in 3D

In our previous work [23], we have investigated heterogeneous nucleation in 2D using Models A and B for a single component system. Herein, assuming isotropic interfacial free energy, and utilizing the respective cylindrical symmetry, we extend our study to 3D and binary alloys using the FP thermodynamic model [Eq. (22)]. The respective form of the Euler-Lagrange equation for the phase field is

$$\frac{1}{r}\frac{\partial}{\partial r}\left(r\frac{\partial\phi}{\partial r}\right)+\frac{\partial^2\phi}{\partial z^2}=\frac{G'(\phi)w-p'(\phi)X\Delta c(c_L-c_\infty)}{\varepsilon^2}, \tag{37}$$

where prime stands for differentiation with respect to the argument of the function. This equation has been solved numerically under boundary conditions given by Models A, B, and C ($g = 0$) using the PDE Toolbox of Matlab (@The MathWorks Inc., 1984-2008) that relies on a combination of the finite element and relaxation methods [43]. This approach needs a reasonable guess for the phase field distribution that is sufficiently close to the solution, to be used as the starting distribution for relaxation.

In mapping the properties of nuclei, we have used the following strategy. First, the solution corresponding to semi-wetting case [$\psi = \pi/2$, $\phi_0 = 0.5$, $h = 0$, respectively in Models A, B, and C ($g = 0$)] has been determined. The initial phase

field distribution used here was $\phi(r) = ½ \{1 - \tanh[(r - R_{CNT})/d_0]\}$, where $R_{CNT} = 2\gamma_{LS}/[X\Delta c(c_L - c_\infty)]$ and $d_0 = d_{10\text{-}90\%}/\ln(0.9/0.1)$ are the classical radius of nuclei and an interface thickness parameter, expressed in terms of the 10% – 90% interface thickness. Having found the respective solution by the relaxation method, the mapping property (ψ, ϕ_0, h, supersaturation, etc.) has been changed in small increments, so that the solution for the previous computation could be used as a suitable starting distribution for the next computation.

For Models A and C ($g = 0$), the free energy of formation of nuclei has been calculated as

$$W_{A,C} = F[\phi_1^*(r)] - F[\phi_0^*(r)] - \int_S dA\{\gamma_W(\phi) - \gamma_{WL}\}, \tag{38}$$

where the first two terms represent the volumetric contribution, while the third term account to the change of the surface function. Here $\gamma_W(\phi) - \gamma_{WL} = -\gamma_{SL}\cos(\psi)\,[2\phi^3 - 3\phi^2 + 1]$ [23], while $\phi_1^*(\mathbf{r})$ is the solution corresponding to the nucleus, and $\phi_0^*(\mathbf{r})$ is the solution without nucleus (liquid of the initial composition in contact with the wall). The latter solution has been obtained the same way as the one for the nucleus, however, using a homogeneous bulk liquid in contact with the wall as the starting condition.

In Model B, there is no contribution from the interface function, thus

$$W_B = F[\phi_1^*(r)] - F[\phi_0^*(r)] \tag{39}$$

applies.

We have investigated the properties of nuclei at a high supersaturation ($S = 5.0$). The free energy of formation of the heterogeneous nuclei relative to the free energy of formation of the respective classical (sharp interface) homo geneous solution is shown for Models A, B, and C ($g = 0$) in Figs. 7-9, respectively.

One observes remarkable differences in the shape of the contour lines the three models predict. In *Model A* (Fig. 7), the contour lines corresponding to phase field levels of 0.1, 0.2, 0.3, 0.4, 0.5, 0.6, 0.7, 0.8, and 0.9 (when they appear), are roughly concentric circles, of which those for $\phi \leq 0.5$ intersect the wall. The contour line $\phi = 0.5$ approximates well the nominal (equilibrium) contact angle. Accordingly, Model A can indeed be viewed as a diffuse interface realization of the classical spherical cap model (a diffuse solid-liquid interface combined with a sharp wall). At this undercooling, the radius of curvature of the particle is several times larger than the interface width. Accordingly, the behavior of the classical spherical cap model is recovered quite accurately. For example, W/W_{CNT} from the phase field computations approximates closely the catalytic potency factor $f(\psi)$ (see lowermost panel in Fig. 7).

In *Model B* (Fig. 8), only a single contour line intersects the wall, the one corresponding to ϕ_0, while the others are either closed ($\phi > \phi_0$) or open ($\phi < \phi_0$). Accordingly, one can define a contact angle for only the contour line $\phi = \phi_0$. The contact angle defined this way, however, depends strongly on the applied supersaturation, and converges to $\psi = 0$ as the respective critical liquid composition (that depends on ϕ_0 as shown in Fig. 4) is approached. Accordingly, at a fixed supersaturation, the W/W_{CNT} vs ϕ_0 curve reaches zero (ideal wetting) at a finite ϕ_0 value (see lowermost panel in Fig. 8), where the actual liquid composition is the critical composition (given by the relationship shown in Fig. 4).

In the case of *Model C (g = 0)* (Fig. 9), the situation resembles to that seen for Model B, though it is somewhat more complex: there are closed contour lines, and also open ones; however, they are separated by not a single contour line that intersects the wall, as in Model B, but by a range of such contour lines. Phase field values out of the [0, 1] range can be observed at the interface if $h \neq 0$ as predicted in Section IV.A.2 ($\phi < 0$ values at the wall-liquid interface if $h > 0$; $\phi > 0$ values at the wall-solid interface if $h < 0$). These local states at the wall cannot be found in the bulk solid and liquid phases, though they are temporarily accessible in the bulk phases via thermal fluctuations.

The W/W_{CNT} vs h relationship is shown in the lowermost panel of Fig. 9. Interestingly, in the supersaturated state h can reach lower values than allowed in equilibrium. Also, the maximum value for the nucleation barrier may exceed that for homogeneous nucleation. The latter finding suggests that Model C ($g = 0$) can capture walls that prevent nucleation in their neighborhood [44]. Such walls represent a foreign matter that enforces a local structure on the liquid, which is incommensurable with the crystal structure to which the liquid structure transforms during freezing. This might have interesting consequences: Nanoporous materials of walls of this kind could stabilize the liquid state in the pores at temperatures, where otherwise the liquid would freeze.

For fixed model parameter values (ψ, ϕ_0, and h) corresponding to the same equilibrium contact angle, we have computed the nucleation barrier as a function of supersaturation. The results are compared in Fig. 10. For all the models, we find that for $S \rightarrow 0$ the ratio of the nucleation barrier to the corresponding classical spherical cap result (W/W_{SC}) tends to 1, i.e., with increasing size the phase field results converge to the classical spherical cap model. In the cases of Models A and B, the nucleation barrier decreases monotonically with an increasing driving force, and for Model B it converges to 0 at a ϕ_0-dependent critical supersaturation (for the dependence see Fig. 5). In contrast, in Model C ($g = 0$), the W vs. S relationship shows a maximum, before the barrier height decreases to 0 at an h-dependent critical supersaturation (for the dependence, see Fig. 6). For $h > 0$ there is no critical supersaturation in Model C, and W decreases monotonically with increasing driving force S, although W/W_{SC} increases.

We note here that in many gradient theories one has a spinodal point between the highly undercooled bulk liquid and the crystalline phase [45] (though usually it falls into the non-physical regime, e.g. to a negative temperature). The existence of

such a spinodal point and its influence on nucleation has been the subject of extensive discussions [46,47], especially for short range interactions (see [46] for review). Recent atomistic simulations seem to imply that no convincing evidence is available for the existence of such a spinodal point [48]. With the present choice of G(ϕ) and $p(\phi)$, this crystal-liquid spinodal falls to the $S \to \infty$ limit, well beyond the boundary of the physically accessible range $S_{max} = 6.9474$ corresponding to $c_\infty = 0$.

C. Formation of complex structures via heterogeneous nucleation

1. Shish-kebab structure in Model A

Here, we present polycrystalline structures obtained relying on the quaternion representation of local crystallographic orientation, Pusztai *et al*. [26] proposed recently. For the sake of illustrating the capabilities of advanced phase field modeling that relies on noise-induced heterogeneous nucleation on external walls, we simulate the shish-kebab structure seen to form on carbon nanotubes in polymeric systems [38]. To accomplish this, we have introduced curved tubes into the simulation box generated so that the local (gradually changing) crystallographic orientation lies in the axis of the tube, whose shape has been constructed stepwise, so that its direction in the next segment might deviate from the orientation of the previous segment by only a small random angle. The contact at the wall of the nanotubes is characterized by Eq. (14), while prescribing a contact angle of $\psi = \pi/4$.

Illustrative simulations have been performed for a hypothetic binary system, whose phase diagram and thermodynamic properties are similar to those of the Ni-Cu system, approximated by the regular solution model, applied in previous work [21]. (Application for real polymer blends of known Gibbs free energy functions should be straight-forward.) Unlike, the metallic systems, polymers often crystallize in the form of disc-like flakes. To mimic this behavior, we have introduced an anisotropic form for the phase field mobility, which prefers the formation of disc-like growth forms (see Fig. 2).

The simulation has been performed on a $200 \times 200 \times 300$ cubic grid with spatial and time steps of $\Delta x = 10$ nm and $\Delta t = 10$ ns at the initial liquid concentration of $c_{Ni} = 0.4192$. Snapshots of the simulation are shown in Fig. 11. Note the similarity to the experimental structures reported in Ref. 38.

2. Columnar to equiaxed transition in Model A

Another illustration that shows the capabilities of phase field simulations incorporating heterogeneous nucleation is the application of Model A for describing the columnar to equiaxed transition (a work done in the framework of the EU FP6 IMPRESS project [49]). Here, we have combined Model A with a 3D model of polycrystalline solidification relying on the quaternion representation of the crystallographic orientations [26] and adopted it to constant temperature gradient and a moving frame. To enable large scale simulations, we have used a broad interface (of thickness 65.6 nm), and included an

anti-trapping current [50] to ensure a quantitative description of growth kinetics. In the simulation window, the material is made to move with a homogeneous velocity from right to left, while a fixed temperature gradient is prescribed in the horizontal direction. Particles of given number density, of random orientation and size, and of given contact angle enter into the simulation window at the right edge, while periodic boundary condition is used on the horizontal edges.

Snapshots of the chemical and orientation maps illustrating polycrystalline solidification under such conditions are presented in Fig. 12. As a result of the diminishing nucleation rate due to the increasing contact angle, we observe a gradual transition from the equiaxed polycrystalline structure to a columnar structure. A more detailed analysis of this phenomenon will be presented elsewhere [51].

3. The liquid-solid meniscus position in Model B

As demonstrated above, if we fix the value of the phase field at a wall to $\phi = \phi_0$, a contact angle will result. Specifically, at the wall, the expression for the contact angle is $\cos(\psi) = 2\phi_0^2(3 - 2\phi_0) - 1$. This can be realized numerically by fixing the value of the phase field at $\phi = \phi_0$ everywhere in the "wall" material. To illustrate this approach we have done a few sample calculations of capillary rise under circumstances that favor either wetting or dewetting. Using our model, we are able to investigate the evolution of a column of liquid-solid and between two wetting interfaces, and compare the predictions with the analysis made above. We choose to do calculations in an insulating box (no change in the total mass of the system), with $\varepsilon^2 = 4.95 \times 10^{-9}$ J/m, and $w = 3.96 \times 10^8$ J/m^3, as is done in the simulations with particles shown above. Fig. 13 shows two typical simulations, with box sizes of 22.8 nm × 22.8 nm, with 100 × 100 grid resolution, and 20% of the box on the left and right occupied by wall material. We consider the symmetric cases of $\phi_0 = 0.3$ [Figs. 13(a) and (b)] and $\phi_0 = 0.7$ [Figs. 13(c) and (d)], corresponding to solid-wall contact angles of $\psi = 124.61°$ and $\psi = 55.39°$, respectively. We start with a system at a uniform concentration that guarantees that the final interface position remains in the box, which, for these choices of contact angle, is satisfied by $S = 1.0$ and 0.2 respectively. The figure shows the calculation initially, and after it has come to equilibrium (1 ms).

To get an estimate of the equilibrium configuration of the meniscus, one can use a simple mass conservation argument to show that

$$H_S = WS + \frac{l}{4}\left[\frac{\psi - \cos\psi \sin\psi}{\sin^2\psi}\right], \tag{40}$$

where H_S is the height at the center of the solid meniscus from the bottom of the column, W is the width of the column, and l is the height of the entire column, the bracketed quantity accounts for the circular cap of liquid or solid, and S is here the su-

persaturation, *uncorrected for curvature*. To improve on the estimate, the supersaturation can be corrected, to linear order, by replacing S by $S + 2\,\gamma_{SL}\sin\psi\,/\,(X\Delta c^2\ell)$. Using these relationships the calculations shown in the figure agree with this analysis within 5%, with no substantial improvement if the grid is refined.

For $\phi_0 = 0.3$, the measured value of H_S is 0.625, while the analysis yields 0.603, while for $\phi_0 = 0.7$ H_S converges to 0.628, while the analysis yields 0.597. The estimate could be improved by using a full, non-linear correction to the compositions, as well as a more consideration of the non-classical influence of the finite interface thickness. Clearly, the method is a convenient approach for capturing complex phenomena.

4. Particle-front interaction in Model C

Finally we examine an application of Model C. We consider the same parameters (except that the initial supersaturation is $S = 0.86$) used in the above section, but now examine the passage of an interface through a distribution of interacting particles. The analysis of such a phenomenon is essentially similar to Zener pinning [52], and it is not the intent of this manuscript to fully explore this phenomenon, but instead to demonstrate the flexibility and generality of our approach.

Fig. 14 shows a series of calculations that show the phenomenological richness available within this relatively simple model. We discuss the images in a clockwise sequence. Panels (a)–(c) show the propagation of the solidification front in the presence of foreign particles of circular shape, starting with (a) and proceeding for 6 μs, with a contact angle on the particles set in Model C using $h = -0.05$ [so the equilibrium contact angle defined by Eq. (35) is $\psi \approx 73°$]. The interface eventually arrests, but much of the box solidifies (≈ 71%). In order to examine the influence of shape and wettability, we first examine changing the shape of the drops to "sticks", [seen in panels (d) and (e)] but with the same distribution of particles. We see that for the sticks the interface arrests much more quickly, at a solid fraction of ≈ 39%. Solidification at a reduced wettability $h = -0.025$ (corresponding to $\psi \approx 81°$), is shown in panels (e) to (h). Apparently, this does not alter substantially the solidification front [*cf.* panels (d) and (e)]. Thus we infer that the presence of right angle corners strongly influences the pinning of the interface. In contrast, in frame (f) all that is changed from frame (c) is the contact angle, and we see that the interface now arrests with this modestly higher angle (a solid fraction ≈ 29%), and increasing the size of the droplets [see panel (g)] does not influence the profile substantially (25%, however much of the difference is due to the increased percentage of impurities). Finally, in panel (h), we reduce the size of the particles, and the interface once again is substantially less impeded, with 73% of the liquid solidifying. Clearly, a substantial numerical exploration of this phenomenon could yield further insights into such pinning behavior in real systems, particularly if a physically motivated wall function could be established through either measurement or *ab initio* calculations.

V. SUMMARY

We have presented three possible approaches to model the wetting properties of foreign walls in the framework of phase field simulations for the solidification of binary alloys. These approaches differ in the treatment of the foreign surfaces:

(a) Model A is a diffuse interface realization of the classical spherical cap model with a contact angle that is essentially independent of the driving force ensured by a specific surface function.

(b) Model B is a non-classical formulation that assumes a fixed phase field value at the interface, leading to surface ordering/disordering, a strongly supersaturation dependent contact angle, and to a surface spinodal (ideal wetting beyond a critical supersaturation). In this model, only such local states can be realized at the wall, which are present in the solid-liquid interface.

(c) Model C is a non-classical approach, which in its simplest form ($g = 0$), fixes the normal component of the phase field gradient, leading to surface ordering / disordering, a supersaturation dependent contact angle, and to a surface spinodal, the latter restricted to the $h < 0$ region ($\psi < \pi/2$). This model allows a stable appearance of such local states at the wall that are available in the bulk phases only temporarily in the presence of thermal fluctuations.

Models A, B, and C represent different levels of abstraction as we discussed above, and can be used to address a broad variety problems of including the formation of complex solidification structures, such as the shish-kebab morphology in carbon nanotube filled polymers, the columnar to equiaxed transition and the front-particle interaction in alloys. Any of these models can be used to describe interfaces that are characterized by a given contact angle in equilibrium, however, the behavior predicted in the supersaturated state depends on the individual model.

Comparative studies relying on combined phase field and atomistic simulations are planned to identify the validity range of the individual models and the predicted complex behavior (e.g. the appearance of surface spinodal).

ACKNOWLEDGMENTS

The authors acknowledge helpful discussions with J. W. Cahn, J.E. Guyer, D. M. Saylor and G. B. McFadden. This work has been supported by contracts OTKA-K-62588, ESA PECS Nos. 98043 and 98056, and by the EU FP6 Project IMPRESS under Contract No. NMP3-CT-2004-500635. T. P. acknowledges support by the Bolyai János Scholarship of the Hungarian Academy of Sciences.

DISCLAIMER

The mention of commercial products, their source, or their use in connection with the material reported herein is not to be construed as either an actual or implied endorsement by the National Institute of Standards and Technology.

---

[1] W. Kurz and D. J. Fisher, *Fundamentals of Solidification* (Trans Tech Publ., Switzerland, 1989), Chap. 2.

[2] S. Auer and D. Frenkel, Nature **409**, 1020 (2001); D. Moroni, P. R. ten Wolde, and P. G. Bolhuis, Phys. Rev. Lett. **94**, 235703 (2005).

[3] S. Auer and D. Frenkel, Phys. Rev. Lett. **91**, 015703 (2003).

[4] J. Aizenberg, A. J. Black, and G. M. Whitesides, Nature **398**, 495 (1999); F. Favier, E. C. Walter, M. P. Zach, T. Benter, and R. M. Penner, Science **293**, 2227 (2001); J. D. Hartgelink, E. Beniash, and S. I. Stupp, *ibid.* **294**, 1684 (2001); N. Ravishankar, V. J. Shenoy, and C. B. Carter, Adv. Mater. **16**, 76 (2004); B. P. Grady *et al.* J. Phys. Chem. B **106**, 5852 (2002).

[5] Herring, *The Physics of Powder Metallurgy* (McGrew-Hill, 1951), p. 143.

[6] For review see: (a) D. Bonn and D. Ross, Rep. Prog. Phys. **64**, 1084 (2001); (b) A. Esztermann and H. Löwen, J. Phys.: Condens. Matter **17**, S429 (2005).

[7] J. W. Cahn, J. Chem. Phys. **66**, 3667 (1977); M. R. Moldover and J. W. Cahn, Science **207**, 1073 (1980).

[8] (a) J. D. van der Waals, Verhand. Kon. Akad. v. Wetensch. (Ie Cest.) **1**, 1 (1893); (b) E. M. Blokhuis, Phys. Rev. E **51**, 4642 (1995); (c) B. Widom, J. Phys. Chem. **99**, 2803 (1995); (d) V. Talanquer and D. W. Oxtoby, J. Chem. Phys. **104**, 1483 (1996); (e) L. M. Pismen and Y. Pomeau, Phys. Rev. E **62**, 2480 (2000); (f) B. Husowitz and V. A. Talanquer, J. Chem. Phys. **121**, 8021 (2004); (g) K. Luo, M.-P. Kuittu, C. Tong, S. Majaniemi, and T. Ala-Nissila, J. Chem. Phys. **123**, 194702 (2005).

[9] (a) K. Yasuoka, G. T. Gao, and X. C. Zeng, J. Chem. Phys. **112**, 4279 (2000); (b) A. Milchev, A. Milchev, and K. Binder, Comp. Phys. Comm. **146**, 38 (2002); (c) E. B. Webb III, G. S. Grest, and D. R. Heine, Phys. Rev. Lett. **91**, 236102 (2003).

[10] For example: J. H. Perepezko, Mater. Sci. Eng. A **413**, 389 (2005); J. H. Perepezko and W. S. Tong, Philos. Mag. **361**, 447 (2004).

[11] M. Volmer, Z. Electrochemie **35**, 555 (1929); D. Turnbull, J. Chem. Phys. **18**, 198 (1950).

[12] (a) L. Gránásy, J. Mol. Struct. **485-486**, 523 (1999); (b) L. Gránásy and T. Pusztai, J. Chem. Phys. **117**, 10121 (2002); (c) L. Gránásy, T. Börzsönyi, and T. Pusztai, Phys. Rev. Lett. **88**, 206105 (2002).

[13] For example: *Experiment:* (a) W. J. Huisman, J. F. Peters, M. J. Zwanenburg, S. A. de Wries, T. E. Derry, D. Abernathy, and J. F. van der Veen, Nature **390**, 379 (1997); (b) J. M. Howe and H. Saka, MRS Bull. **29**, 951 (2004). *Atomistic simulations:* (c) B. B. Laird and A. D. J. Haymet, Chem. Rev. **92**, 1819 (1992); (d) P. Geysermans, D. Gorse, and V. Pontikis, J. Chem. Phys. **113**, 6382 (2000).

[14] J. J. Hoyt, M. Asta, and A. Karma, Mater. Eng. Rep. R **41**, 121 (2003).

[15] L. Gránásy, T. Pusztai, and J A. Warren, J. Phys.: Cond. Matter. **18**, R1205 (2004).

[16] L. Gránásy, T. Pusztai, G. Tóth, Z. Jurek, M. Conti, and B. Kvamme, J. Chem. Phys. **119**, 10376 (2003); G. I. Tóth and L. Gránásy, *ibid.* **127**, 074709, 074710 (2007).

[17] For example: K. R. Elder, F. Drolet, J. M. Kosterlitz, and M. Grant, Phys. Rev. Lett. **72**, 677 (1994); F. Drolet, K. R. Elder, M. Grant, and J. M. Kosterlitz, Phys. Rev. E **61**, 6705 (2000); M. Plapp and M. Karma, Phys. Rev. E **66**, 061608 (2002); B. Nestler and A. A. Wheeler, Physica D **138**, 114 (2000); H. Emmerich and R. Siquieri, J. Phys.: Cond. Matter. **18**, 11121 (2006).

[18] A. Semoroz, S. Henry, and M. Rappaz, Metall. Mater. Trans. **31A**, 487 (2000).

[19] B. P. Athreya, J. A. Dantzig, S. Liu, and R. Trivedi, Philos. Mag. **86**, 3739 (2006).

[20] M. Castro, Phys. Rev. B **67**, 035412 (2003).

[21] L. Gránásy, T. Pusztai, T. Börzsönyi, G. Tóth, G. Tegze, J. A. Warren, and J. F. Douglas, J. Mater. Res. **21**, 309 (2006).

[22] M. Iwamatsu, J. Chem. Phys. **126**, 134703 (2007).

[23] L. Gránásy, T. Pusztai, D. Saylor, and J A. Warren, Phys. Rev. Lett **98**, 035703 (2007).

[24] D. Jacqmin, J. Fluid. Mech. **402**, 57 (2000).

[25] H. Ding and P. D. M. Spelt, Phys. Rev. E **75**, 046708 (2007).

[26] T. Pusztai, G. Bortel, and L. Gránásy, Europhys. Lett. **71**, 131 (2005); *idem*. Mater. Sci. Eng. A **412-413**, 412 (2005).

[27] R. Kobayashi and J. A. Warren, TMS Lett. **2**, 1 (2005); *idem*. Physica A **356**, 127 (2005).

[28] A. Morowiec, *Orientations and Rotations* (Springer-Verlag, Berlin-Heidelberg, 2004).

[29] J. A. Warren and W. J. Boettinger, Acta Metall. Mater. **43**, 689 (1995).

[30] For example: G. Caginalp and J. Jones, Ann. Phys. (N.Y.) **237**, 66 (1995) and papers in Ref. 17.

[31] S. Toxvaerd, J. Chem. Phys. **117**, 10303 (2002).

[32] E. B. Webb, G. S. Grest, and D. R. Heine, Phys. Rev. Lett. **91**, 236102 (2003).

[33] R. Folch and M. Plapp, Phys. Rev. E **68**, 010602 (2003); **72**, 011602 (2005).

[34] M. Tang, W. C. Carter, and R. M. Cannon, Phys. Rev. Lett. **97**, 075502 (2006).

[35] Note that due to the lack of a $|\nabla c|^2$ term in the free energy functional, the Euler-Lagrange equation for the concentration field [Eq. (7)] boils down to an explicit relationship between c and ϕ. In equilibrium, $\Delta f\,[\phi, c(\phi)]$ has a double-well form. In the parabolic free energy well approximation of Folch and Plapp (Ref. 33), it comes exclusively from the term $Wg(\phi)$. Generally, however, there are other ϕ-dependent contributions from the composition dependent part too.

[36] L. Gránásy, T. Pusztai, J. A. Warren, T. Börzsönyi, J. F. Douglas, V. Ferreiro, *Nature Mater.* **2**, 92 (2003); L. Gránásy, T. Pusztai, T. Börzsönyi, J. A. Warren, J. F. Douglas, Nature Mater. **3**, 635 (2004).

[37] L. Gránásy and M. Tegze, Mater. Sci. Forum **77**, 243 (1991).

[38] C. Y. Li, L.-Y. Li, W.-W. Cai, S. L. Kodjie, and K. K. Tenneti, Adv. Mater. **17**, 1198 (2005).

[39] R. Kobayashi and Y. Giga, Jpn. J. Industrial Appl. Math. **18**, 207 (2001).

[40] A. Dinsdale, personal communication.

[41] T. Pusztai, G. Bortel, and L. Gránásy, *Modeling of Casting, Welding and Advanced Solidification Processes - XI* ed C A Gandin and M Bellet (The Minerals, Metals and Materials Society, Warrendale, 2006) p. 409.

[42] J. W. Cahn and J. E. Hilliard, J. Chem. Phys. **28**, 258 (1958).

[43] MATLAB: Partial Differential Equation Toolbox 1, User's Guide (The MathWorks Inc., Natick, 2008).

[44] Structured walls that disfavor crystallization via enforcing a fivefold symmetry have been seen in atomistic simulations: M. Heni and H. Löwen, Phys. Rev. E **65**, 021501 (2002), and Ref. 6(b).

[45] For example: C. K. Bagdassarian and D. W. Oxtoby, J. Chem. Phys. **100**, 2139 (1994); M. Iwamatsu and K. Horii, J. Phys. Soc. Jpn. **65**, 2311 (1996); *ibid.* **66**, 1210 (1997); L. Gránásy, J. Mol. Struct. **485-486**, 523 (1999); L. Gránásy and D.W. Oxtoby, J. Chem. Phys. **112**, 2399 (2000).

[46] J. D. Gunton, M. San Miguel, and P. S. Sahni, Phase Transitions and Critical Phenomena, Vol. 8, eds. C. Domb and J. L. Lebowitz (Academic, New York, 1983) p. 267.

[47] For example: W. Klein, and F. Leywraz, Phys. Rev. Lett. **57**, 2845 (1986); C. J. Gagne, H. Gould, W. Klein, T. Lookman, and A. Saxena, Phys. Rev. Lett. **95**, 095701 (2005); H. Wang, H. Gould, and W. Klein, Phys. Rev. E **76**, 031604 (2007) ; F. Trudu, D. Donadio, and M. Parrinello, Phys. Rev. Lett. **97**, 105701 (2007); L. S. Bartell and D. T. Wu, J. Chem. Phys. **127**, 174507 (2007).

[48] L. S. Bartell and D. T. Wu, J. Chem. Phys. **127**, 174507 (2007); L. J. Peng, J. R. Morris, and Y. C. Lo, Phys. Rev. B **78**, 012201 (2008).

[49] D. J. Jarvis and D. Voss, Mater. Sci. Eng. A **413-414** 583 (2005).

[50] A. Karma, Phys. Rev. Lett. **87**, 115701 (2001); S. G. Kim, Acta Mater. **55**, 4391(2007).

[51] T. Pusztai, L. Környei, and L. Gránásy, unpublished.

[52] See for example: C.S. Smith, Trans. Am. Inst. Mineral Eng. **175**, 15 (1948); G. Couturier, R. Doherty, C. Maurice, and R. Fortunier, Acta Mater. **53**, 977 (2005); M. A. Miodownik, in Encyclopedia of Materials: Science and Technology, Eds. K.H. Buschow, R.W. Cahn, M.C. Fleming, B. Ilschner, E.J. Kramer, S. Mahajan, and P. Veyssière (Elsevier, Amsterdam, 2008) p. 9855.

FIGURE CAPTIONS

FIG. 1: Definition of contact angle, ψ: glycerin droplet on glass surface.
http://lejpt.academicdirect.org/A10/029_038_files/image009.jpg)

FIG. 2: (a) Kinetic anisotropy used in simulations for the polymer-carbon nanotube mixture and (b) the respective asymptotic growth form (kinetic Wulff shape [38]).

FIG. 3: (a) Anisotropy of the interfacial free energy used in simulations for columnar to equiaxed transition in the Al-Ti alloy and (b) the respective asymptotic growth form (kinetic Wulff shape [38]).

FIG. 4: A plot of contact angle as a function of parameter h in Model C ($g = 0$). For $h < -0.1703$ the contact angle is 0, while for $h > 0.1703$, it is π.

FIG. 5: Critical liquid supersaturation corresponding to ideal wetting as a function of phase field value ϕ_0 at the wall in Model B at $T = 1574$ K for Cu-Ni with a physical interface thickness of 1 nm. The horizontal dashed line shows the maximum possible supersaturation $S_{max} = 6.9474$ (corresponding to $c_\infty = 0$). Results above this line are unphysical.

FIG. 6: Critical liquid supersaturation corresponding to ideal wetting as a function of $-h$ at the wall in Model C ($g = 0$) at $T = 1574$ K for Cu-Ni with a physical interface thickness of 1 nm. The horizontal dashed line shows the maximum possible supersaturation $S_{max} = 6.9474$ (corresponding to $c_\infty = 0$). Results above this line are unphysical.

FIG. 7: Structure of heterogeneous nuclei at $S = 5.0$ in Model A at various contact angles (upper and central row)). There is a symmetry plane on the left edge. The contour lines vary between 0.1 and 1.0 by increments of 0.1: $\phi = 0.1, 0.2, \ldots, 0.9$. Note that these lines correspond to local supersaturations of $S = 0.1, 0.2, \ldots, 0.9$. The

lowermost panel shows the ratio of the PF prediction for the nucleation barrier height (circles) normalized by the barrier height for the homogeneous nucleus in the droplet model of the classical nucleation theory. For comparison, the catalytic potency factor $f(\psi)$ from the spherical cap model is also shown (solid line).

FIG. 8: Structure of heterogeneous nuclei at S = 5.0 in Model B at various phase field values at the wall (upper and central row)). The contour lines vary between 0.1 and 1.0 by increments of 0.1: ϕ = 0.1, 0.2, … , 0.9. Note that these lines correspond to local supersaturations of S = 0.1, 0.2, … ,0.9. The lowermost panel shows the ratio of the PF prediction for the nucleation barrier height (circles) normalized by the barrier height for the homogeneous nucleus in the droplet model of the classical nucleation theory. For comparison, the catalytic potency factor $f(\psi)$ from the spherical cap model is also shown (solid line).

FIG. 9: Structure of heterogeneous nuclei at S = 5.0 in Model C (g = 0) at various values of the model parameter h (upper and central row)). The contour lines vary between 0.1 and 1.0 by increments of 0.1: ϕ = 0.1, 0.2, … , 0.9. Note that these lines correspond to local supersaturations of S = 0.1, 0.2, … ,0.9. The lowermost panel shows the ratio of the PF prediction for the nucleation barrier height normalized by the barrier height for the homogeneous nucleus in the droplet model of the classical nucleation theory (circles). For comparison, the catalytic potency factor $f(\psi)$ from the spherical cap model is also shown (solid line). The deviation of the background hue from white in panels for $h > 0$ indicates that negative ϕ and S values appear in the vicinity of the wall, where it is contact with the liquid phase.

FIG. 10: Nucleation barrier height (W) normalized by that from the classical spherical cap model (W_{SC}) vs. supersaturation (S) for Models A (square), B (triangle), and C (diamond) at interface parameters ψ = 60°, ϕ_0 = 0.673648 and h = –0.083733, respectively, which all realize the same equilibrium contact angle. Note that for both Models B and C (for $h < 0$), there exists a critical supersaturation, where ideal wetting switches in (the nucleation barrier disappears). This critical supersaturation S_c depends on the respective interfacial parameter (ϕ_0 or h). Such surface spinodal-like behavior has not been observed for Model A that realizes the nominal contact angle ψ fairly accurately even at high supersaturations (for Model A the deviation from W/W_{SC}.= 1 originates dominantly from the fact that at large supersaturationa, the height of heterogeneous nuclei becomes comparable to

the interface thickness, and thus there are no bulk crystal properties in the nuclei). The vertical dash-dot line indicates the border S_{max} of the physically accessible region ($S \leq S_{max}$).

FIG. 11: Formation of shish-kebab structure by noise induced heterogeneous nucleation on tubular walls of contact angle $\psi = \pi/4$ in Model A [Eq. (14)] at T = 1574 K and c_{Ni} = 0.4192, in a hypothetical system whose thermodynamic properties are given by an ideal solution approximation of the Cu-Ni system, while its kinetic anisotropy (anisotropy of the phase field mobility) and growth shape are shown in Fig. 2. Snapshots taken at times t = 30, 40, 50, and 60 μs show the walls and the solidification front (ϕ = 0.5). The computations have been performed on a 200 × 200 × 300 grid (2 μm × 2 μm × 3 μm).

FIG. 12: Phase-field simulation of columnar to equiaxed transition in the $Al_{0.45}Ti_{0.55}$ alloy as a function of contact angle of foreign particles in a moving frame (V = 1.26 cm/s) and a constant temperature gradient ($\nabla T = 1.12 \times 10^7$ K/m) in Model A [Eq.(14)]. Composition (on the left) and orientation maps (on the right) corresponding to contact angles of ψ = 30°, 60°, 90°, and 120° (from top to bottom, respectively) are shown. The computations have been performed by solving the 3D phase field model of polycrystalline solidification [26] in 2D on a 600 × 3000 grid (3.93 μm × 19.68 μm). White spots in the chemical map indicate the foreign particles, whose diameter varies in the 13 nm – 66 nm range. In order to be able to distinguish the orientation of the foreign particles, the fluctuating orientation field of the liquid is not shown in the orientation map [color map is multiplied by $p(\phi)$].

FIG. 13: Time evolution of solid-liquid meniscus at vertical walls in Model B for (a),(b) wetting (ψ = 55.39°) and (c),(d) non-wetting (ψ = 124.61°) walls. The phase field map is shown [white – bulk solid (ϕ = 1); black – bulk liquid (ϕ = 0)]. The computations have been performed for Cu-Ni, assuming a 5 nm thick solid-liquid interface. The software tool FiPy was used for the calculations (http://www.ctcms.nist.gov/fipy).

FIG. 14: Particle-front interaction in Model C at a fixed initial liquid supersaturation S = 0.86. Pinning of solidification front to foreign particles: (a)-(c) Propagation and pinning of the solidification front in the presence of circular foreign particles. (d),(e) The effect of shape and contact angle on front-pinning. (f)-(h) The effect of par-

ticle size on the front-pinning. For discussion, see the text. The computations have been performed for Cu-Ni, assuming a 5 nm thick solid-liquid interface. Images (a)-(c) have been computed with $h = -0.05$, while (e)-(f) with $h = -0.025$. (Black – solid; white – liquid; green – foreign particle.) The software tool FiPy was used for the calculations (http://www.ctcms.nist.gov/fipy).

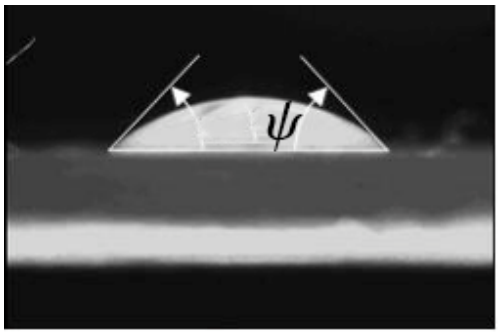

FIG. 1: Definition of contact angle, ψ: glycerin droplet on glass surface.

(http://lejpt.academicdirect.org/A10/029_038_files/image009.jpg)

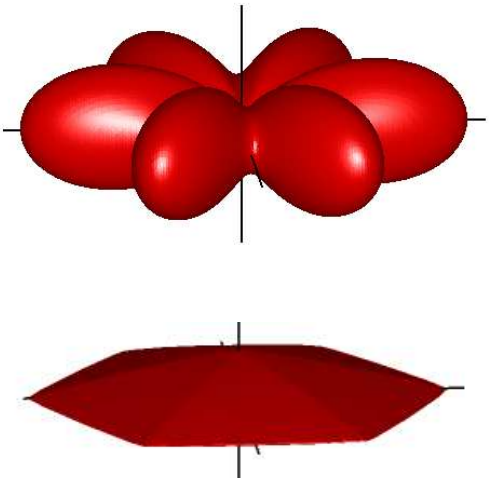

FIG. 2: (a) Kinetic anisotropy used in simulations for the polymer-carbon nanotube mixture and (b) the respective asymptotic growth form (kinetic Wulff shape [38]).

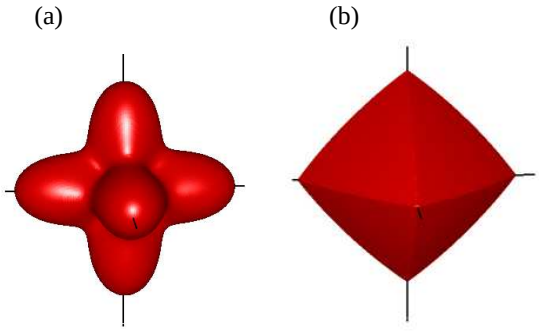

FIG. 3: (a) Anisotropy of the interfacial free energy used in simulations for columnar to equiaxed transition in the Al-Ti alloy and (b) the respective asymptotic growth form (kinetic Wulff shape [38]).

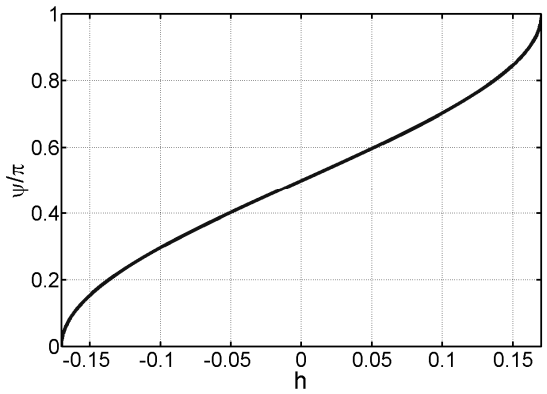

FIG. 4: A plot of contact angle as a function of parameter h in Model C ($g = 0$). For $h < -0.1703$ the contact angle is 0, while for $h > 0.1703$, it is π.

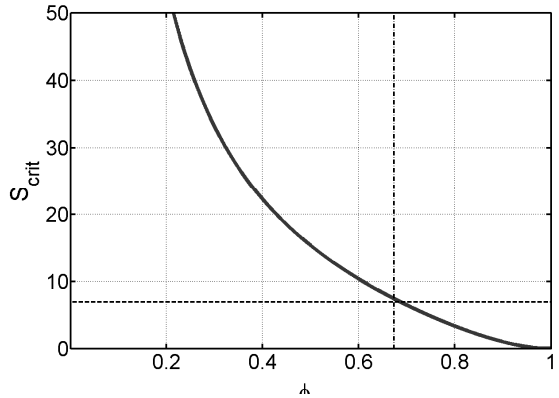

FIG. 5: Critical liquid supersaturation corresponding to ideal wetting as a function of phase field value ϕ_0 at the wall in Model B at T = 1574 K for Cu-Ni with a physical interface thickness of 1 nm. The horizontal dashed line shows the maximum possible supersaturation S_{max} = 6.9474 (corresponding to c_∞ = 0). Results above this line are unphysical.

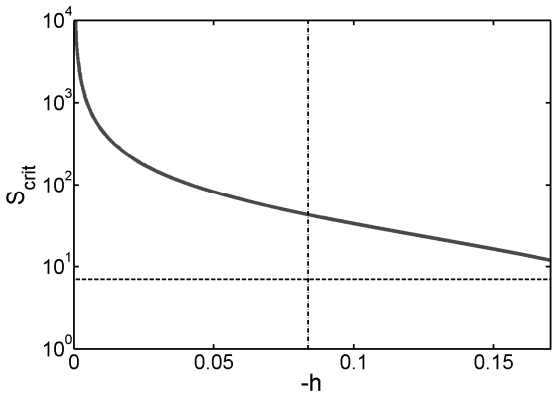

FIG. 6: Critical liquid supersaturation corresponding to ideal wetting as a function of $-h$ at the wall in Model C (g = 0) at T = 1574 K for Cu-Ni with a physical interface thickness of 1 nm. The horizontal dashed line shows the maximum possible supersaturation S_{max} = 6.9474 (corresponding to c_∞ = 0). Results above this line are unphysical.

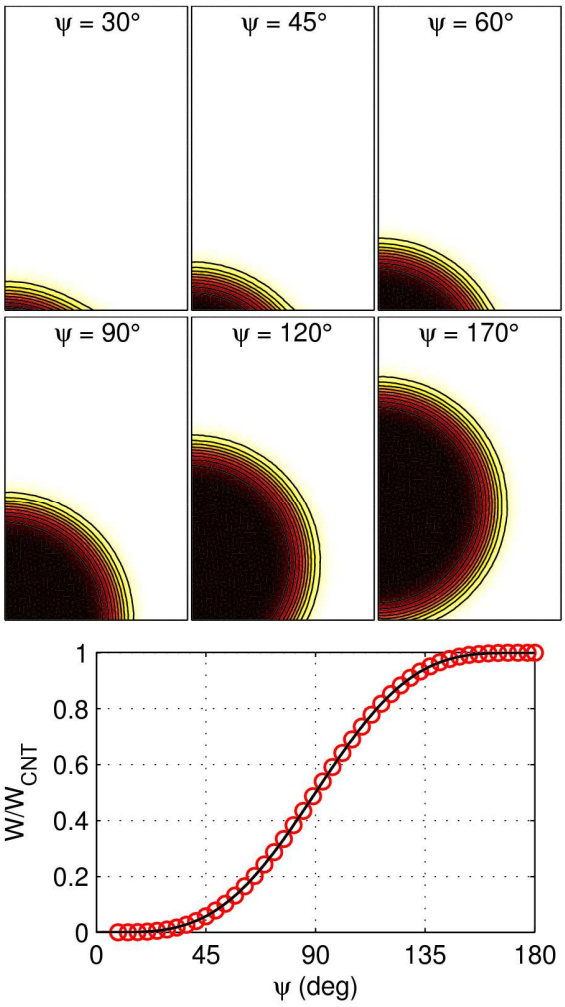

FIG. 7: Structure of heterogeneous nuclei at S = 5.0 in Model A at various contact angles (upper and central row)). There is a symmetry plane on the left edge. The contour lines vary between 0.1 and 1.0 by increments of 0.1: ϕ = 0.1, 0.2, … , 0.9. Note that the respective local supersaturations can be given as $s(\phi) = S + p(\phi)$. The lowermost panel shows the ratio of the PF prediction for the nucleation barrier height (circles) normalized by the barrier height for the homogeneous nucleus in the droplet model of the classical nucleation theory. For comparison, the catalytic potency factor $f(\psi)$ from the spherical cap model is also shown (solid line).

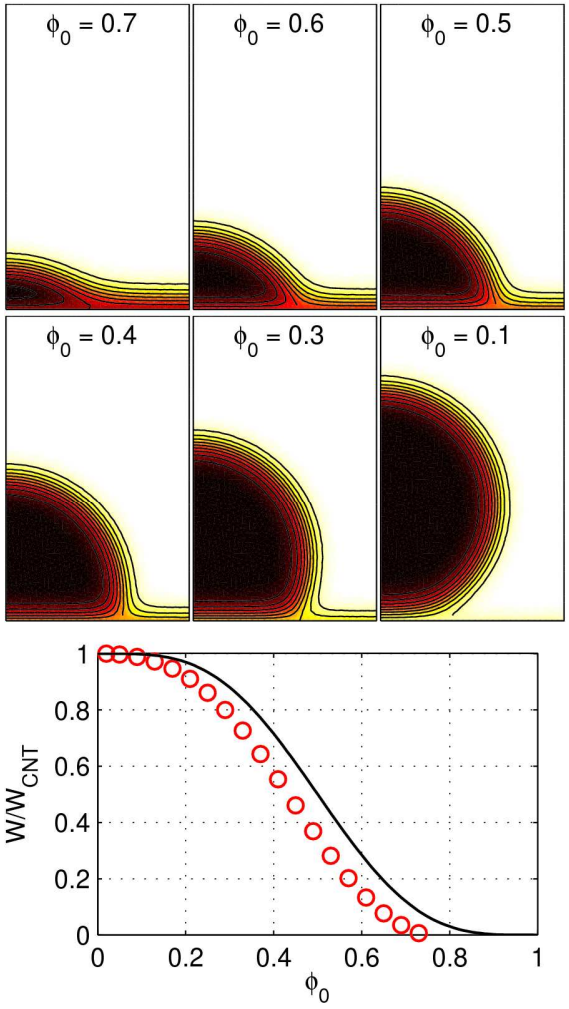

FIG. 8: Structure of heterogeneous nuclei at S = 5.0 in Model B at various phase field values at the wall (upper and central row)). The contour lines vary between 0.1 and 1.0 by increments of 0.1: ϕ = 0.1, 0.2, … , 0.9. Note that the respective local supersaturations can be given as $s(\phi) = S + p(\phi)$. The lowermost panel shows the ratio of the PF prediction for the nucleation barrier height (circles) normalized by the barrier height for the homogeneous nucleus in the droplet model of the classical nucleation theory. For comparison, the catalytic potency factor $f(\psi)$ from the spherical cap model is also shown (solid line).

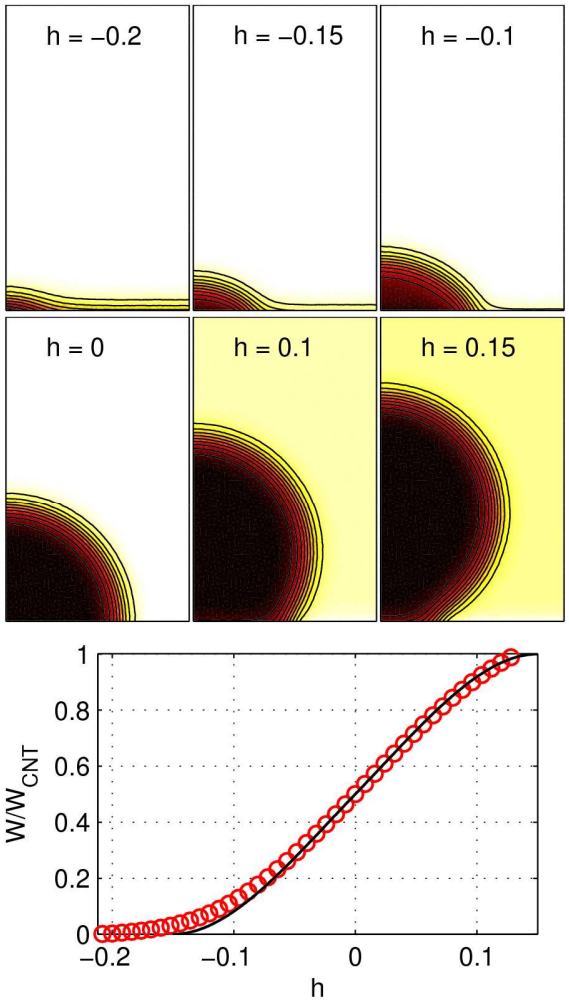

FIG. 9: Structure of heterogeneous nuclei at $S = 5.0$ in Model C ($g = 0$) at various values of the model parameter h (upper and central row)). The contour lines vary between 0.1 and 1.0 by increments of 0.1: $\phi = 0.1, 0.2, \ldots, 0.9$. Note that the respective local supersaturations can be given as $s(\phi) = S + p(\phi)$. The lowermost panel shows the ratio of the PF prediction for the nucleation barrier height normalized by the barrier height for the homogeneous nucleus in the droplet model of the classical nucleation theory (circles). For comparison, the catalytic potency factor $f(\psi)$ from the spherical cap model is also shown (solid line). The deviation of the background hue from white in panels for $h > 0$ indicates that negative ϕ and $s < S$ values appear in the vicinity of the wall, where it is contact with the liquid phase.

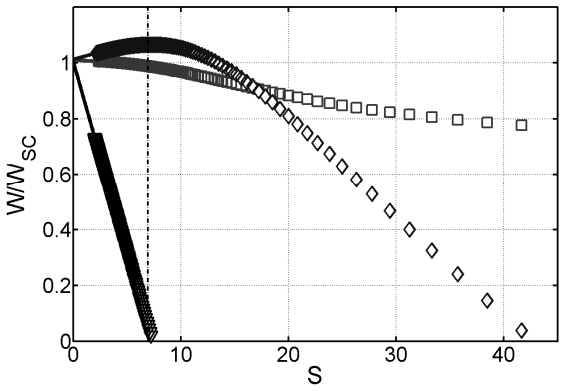

FIG. 10: Nucleation barrier height (W) normalized by that from the classical spherical cap model (W_{SC}) vs. supersaturation (S) for Models A (square), B (triangle), and C (diamond) at interface parameters ψ = 60°, ϕ_0 = 0.673648 and h = –0.083733, respectively, which all realize the same equilibrium contact angle. Note that for both Models B and C (for $h < 0$), there exists a critical supersaturation, where ideal wetting switches in (the nucleation barrier disappears). This critical supersaturation S_c depends on the respective interfacial parameter (ϕ_0 or h). Such surface spinodal-like behavior has not been observed for Model A that realizes the nominal contact angle ψ fairly accurately even at high supersaturations (for Model A the deviation from W/W_{SC}.= 1 originates dominantly from the fact that at large supersaturationa, the height of heterogeneous nuclei becomes comparable to the interface thickness, and thus there are no bulk crystal properties in the nuclei). The vertical dash-dot line indicates the border S_{max} of the physically accessible region ($S \leq S_{max}$).

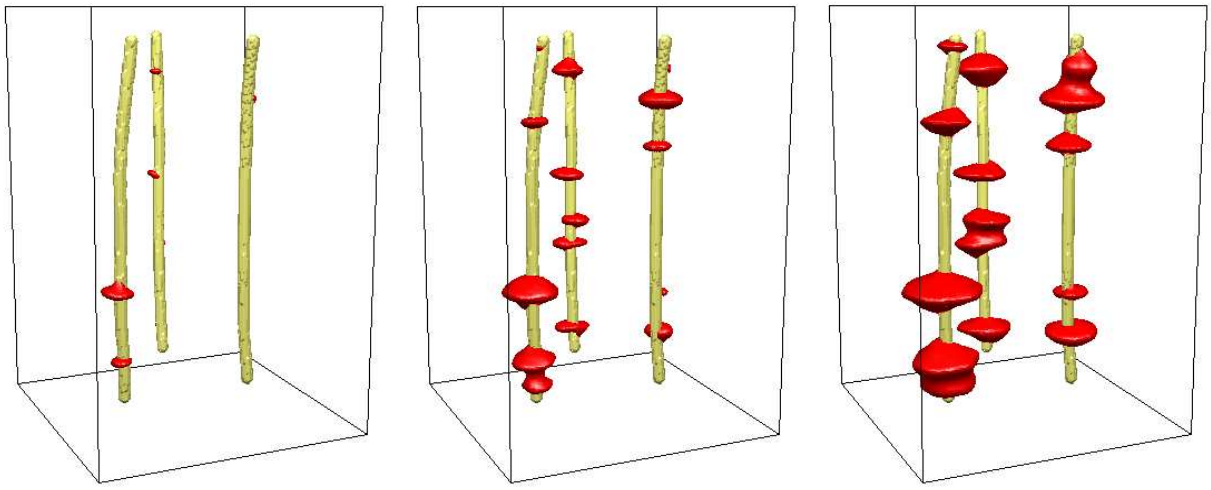

FIG. 11: Formation of shish-kebab structure by noise induced heterogeneous nucleation on tubular walls of contact angle $\psi = \pi/4$ in Model A [Eq. (14)] at T = 1574 K and c_{Ni} = 0.4192, in a hypothetical system whose thermodynamic properties are given by an ideal solution approximation of the Cu-Ni system, while its kinetic anisotropy (anisotropy of the phase field mobility) and growth shape are shown in Fig. 2. Snapshots taken at times t = 30, 40, 50, and 60 μs show the walls and the solidification front (ϕ = 0.5). The computations have been performed on a $200 \times 200 \times 300$ grid (2 μm × 2 μm × 3 μm).

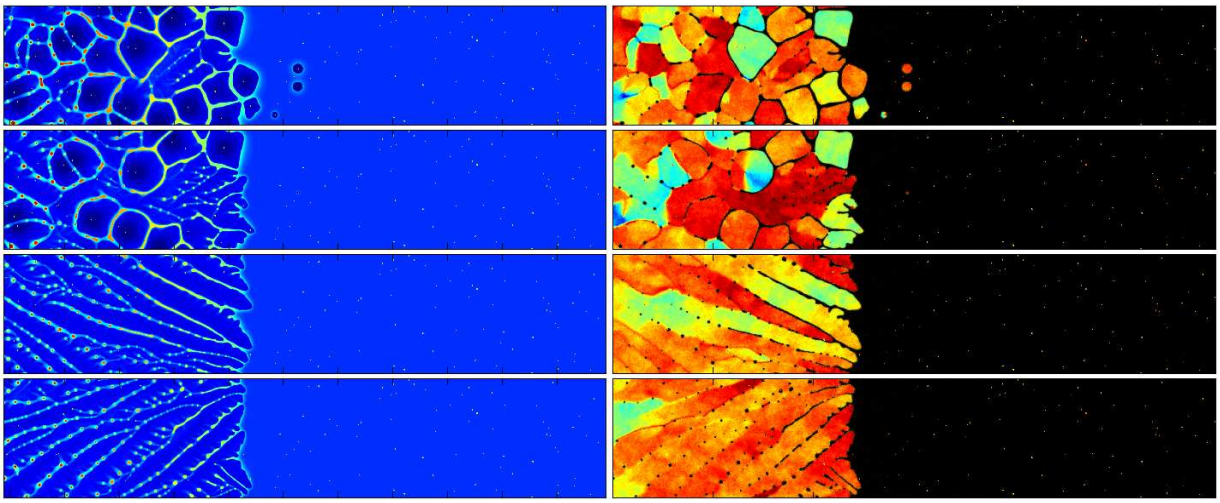

FIG. 12: Phase-field simulation of columnar to equiaxed transition in the $Al_{0.45}Ti_{0.55}$ alloy as a function of contact angle of foreign particles in a moving frame (V = 1.26 cm/s) and a constant temperature gradient ($\nabla T = 1.12 \times 10^7$ K/m) in Model A [Eq.(14)]. Composition (on the left) and orientation maps (on the right) corresponding to contact angles of ψ = 30°, 60°, 90°, and 120° (from top to bottom, respectively) are shown. The computations have been performed by solving the 3D phase field model of polycrystalline solidification [26] in 2D on a 600 × 3000 grid (3.93 μm × 19.68 μm). White spots in the chemical map indicate the foreign particles, whose diameter varies in the 13 nm – 66 nm range. In order to be able to distinguish the orientation of the foreign particles, the fluctuating orientation field of the liquid is not shown in the orientation map [color map is multiplied by $p(\phi)$].

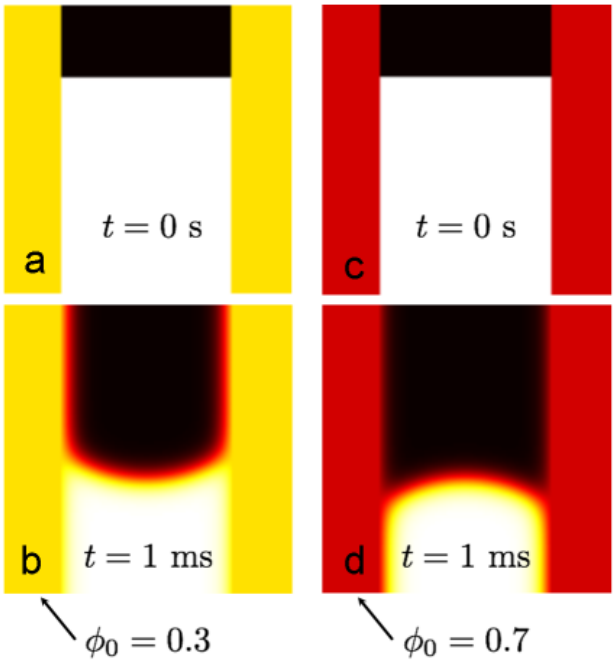

FIG. 13: Time evolution of solid-liquid meniscus at vertical walls in Model B for (a),(b) wetting (ψ = 55.39°) and (c),(d) non-wetting (ψ = 124.61°) walls. The phase field map is shown [white – bulk solid (ϕ = 1); black – bulk liquid (ϕ = 0)]. The computations have been performed for Cu-Ni, assuming a 5 nm thick solid-liquid interface. The software tool FiPy was used for the calculations (http://www.ctcms.nist.gov/fipy).

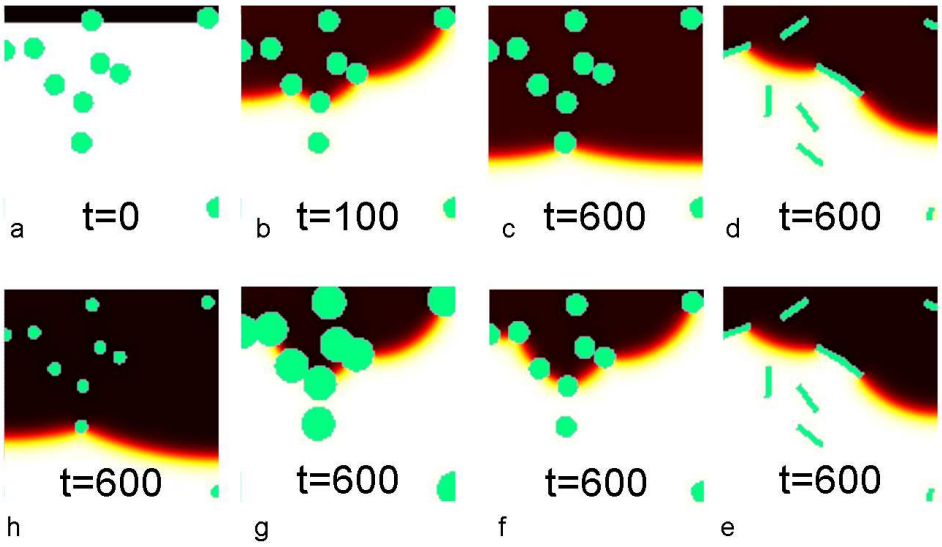

FIG. 14: Particle-front interaction in Model C at a fixed initial liquid supersaturation S = 0.86. Pinning of solidification front to foreign particles: (a)-(c) Propagation and pinning of the solidification front in the presence of circular foreign particles. (d),(e) The effect of shape and contact angle on front-pinning. (f)-(h) The effect of particle size on the front-pinning. For discussion, see the text. The computations have been performed for Cu-Ni, assuming a 5 nm thick solid-liquid interface. Images (a)-(c) have been computed with $h = -0.05$, while (e)-(f) with $h = -0.025$. (Black – solid; white – liquid; green – foreign particle.) The software tool FiPy was used for the calculations (http://www.ctcms.nist.gov/fipy).